

# Lawrence Berkeley National Laboratory

## LBL Publications

### Title

Imaging the Breakdown and Restoration of Topological Protection in Magnetic Topological Insulator MnBi<sub>2</sub>Te<sub>4</sub>

### Permalink

<https://escholarship.org/uc/item/0072p8nn>

### Journal

Advanced Materials, 36(24)

### ISSN

0935-9648

### Authors

Li, Qile  
Di Bernardo, Iolanda  
Maniatis, Johnathon  
[et al.](#)

### Publication Date

2024-06-01

### DOI

10.1002/adma.202312004

### Copyright Information

This work is made available under the terms of a Creative Commons Attribution-NonCommercial-NoDerivatives License, available at <https://creativecommons.org/licenses/by-nc-nd/4.0/>

Peer reviewed

1 Imaging the breakdown and restoration of topological protection in  
2 magnetic topological insulator  $\text{MnBi}_2\text{Te}_4$

3  
4 Qile Li<sup>1,2\*</sup>, Iolanda Di Bernardo<sup>1,2</sup>, Johnathon Maniatis<sup>1</sup>, Daniel McEwen<sup>1,2</sup>, Amelia D.-Celorrio<sup>1,2</sup>,  
5 Mohammad T. H. Bhuiyan<sup>1</sup>, Mengting Zhao<sup>1,2,3</sup>, Anton Tadich<sup>3</sup>, Liam Watson<sup>1,2</sup>, Benjamin Lowe<sup>1,2</sup>,  
6 Thi-Hai-Yen Vu<sup>1</sup>, Chi Xuan Trang<sup>1,2</sup>, Jinwoong Hwang<sup>4,5</sup>, Sung-Kwan Mo<sup>4</sup>, Michael S. Fuhrer<sup>1,2</sup>,  
7 Mark T. Edmonds<sup>1,2,6\*</sup>

8  
9 <sup>1</sup>School of Physics and Astronomy, Monash University, Clayton, VIC, Australia

10 <sup>2</sup>ARC Centre for Future Low Energy Electronics Technologies, Monash University, Clayton, VIC,  
11 Australia

12 <sup>3</sup>Australian Synchrotron, Clayton, VIC, Australia

13 <sup>4</sup>Advanced Light Source, Lawrence Berkeley National Laboratory, Berkeley, CA, 94720 USA

14 <sup>5</sup>Department of Physics and Institute of Quantum Convergence Technology, Kangwon National  
15 University, Chuncheon, 24341, Republic of Korea

16 <sup>6</sup>ANFF-VIC Technology Fellow, Melbourne Centre for Nanofabrication, Victorian Node of  
17 the Australian National Fabrication Facility, Clayton, VIC 3168, Australia

18  
19 \*Corresponding Author [mark.edmonds@monash.edu](mailto:mark.edmonds@monash.edu) and [qile.li@monash.edu](mailto:qile.li@monash.edu)

20  
21 **Abstract –**

22 **Quantum anomalous Hall (QAH) insulators transport charge without resistance along**  
23 **topologically protected chiral one-dimensional edge states. Yet, in magnetic topological**  
24 **insulators (MTI) to date, topological protection is far from robust, with zero-magnetic field QAH**  
25 **effect only realised at temperatures an order of magnitude below the Néel temperature  $T_N$ ,**  
26 **though small magnetic fields can stabilize QAH effect. Understanding why topological**  
27 **protection breaks down is therefore essential to realising QAH effect at higher temperatures.**  
28 **Here we use a scanning tunnelling microscope to directly map the size of exchange gap ( $E_{g,ex}$ )**  
29 **and its spatial fluctuation in the QAH insulator 5-layer  $\text{MnBi}_2\text{Te}_4$ . We observe long-range**  
30 **fluctuations of  $E_{g,ex}$  with values ranging between 0 (gapless) and 70 meV, appearing to be**

31 **uncorrelated to individual surface point defects. We directly image the breakdown of topological**  
32 **protection, showing that the gapless edge state, the hallmark signature of a QAH insulator,**  
33 **hybridizes with extended gapless regions in the bulk. Finally, we unambiguously demonstrate**  
34 **that the gapless regions originate from magnetic disorder, by demonstrating that a small**  
35 **magnetic field restores  $E_{g,ex}$  in these regions, explaining the recovery of topological protection**  
36 **in magnetic fields. Our results indicate that overcoming magnetic disorder is key to exploiting**  
37 **the unique properties of QAH insulators.**

38

39

#### 40 **Main Text-**

41 Topological protection has become a crucial concept in the recent development of condensed matter  
42 physics<sup>1, 2, 3, 4</sup>. In the quantized versions of the Hall effect (QHE), spin Hall effect (QSHE) and  
43 anomalous Hall effect (QAHE), topological protection manifests as one-dimensional electronic edge  
44 states where scattering due to local perturbations is prohibited<sup>5</sup>. This opens the way towards high-  
45 temperature lossless electronic transport applications<sup>6,7</sup> as well as new approaches to topologically-  
46 protected fault-tolerant quantum computing<sup>8, 9</sup>. These technologies require robust topologically  
47 protected edge channels, but in electronic devices this protection is often observed to break down.  
48 Breakdown of the QHE due to disorder, temperature, and current has been understood within scaling  
49 theory<sup>10</sup>, and was a fundamental development in the understanding of continuous quantum phase  
50 transitions<sup>11</sup>. The microscopic origins of disorder-induced QHE breakdown are still a vibrant area of  
51 investigation, with new developments in graphene showing unique aspects of backscattering in the  
52 presence of both electron- and hole-like edge channels<sup>12, 13</sup>. The QSHE is robust to non-magnetic  
53 disorder at zero temperature<sup>14</sup>, but magnetic disorder can cause scattering at finite temperatures<sup>15</sup>, with  
54 a quantum phase transition from helical liquid to insulator under strong interactions<sup>14</sup>. In contrast, the  
55 chiral quantum anomalous Hall (QAH) edge channel supports unidirectional flow of electrical current

56 that should be robust to any potential perturbations smaller than the exchange energy gap  $E_{g,ex}$  which  
57 is opened in the surface-state of a thin film 3D topological insulator (TI) via long-range magnetic order.  
58 <sup>16, 17</sup> Despite this, breakdown of topological protection is ubiquitously observed at far lower  
59 temperatures than  $E_{g,ex}/k_B$  or  $T_N$ , where  $k_B$  is the Boltzmann constant. In dilute magnetic doped  
60 topological insulators, this is thought to be due to magnetic disorder, leading to non-uniform  
61 magnetization and a fragile QAHE that is only observable at extremely low temperatures ( $<1$  K).<sup>18, 19</sup>

62  
63 Intrinsic stoichiometric magnetic topological insulators (MTIs) which possess both non-trivial  
64 topology and intrinsic magnetism, for example  $MnBi_2Te_4$ <sup>20, 21</sup> should in principle circumvent the issues  
65 associated with dilute magnetic doping. Promisingly, odd-layers of  $MnBi_2Te_4$  in the 2D limit host  
66 quantum anomalous Hall states <sup>22</sup>, leading to observation of the QAHE at 1.4 K, with the temperature  
67 increasing to 6.5 K under application of an external magnetic field<sup>23</sup>. Yet, this value is still substantially  
68 lower than  $T_N = 25$  K and the activation energy extracted from transport measurements of  $\Delta E = 0.64$   
69 meV is two orders of magnitude smaller than the predicted  $E_{g,ex} = 70$  meV (800K). Furthermore,  
70 QAHE is not routinely observed in ultra-thin odd-layer  $MnBi_2Te_4$  samples or quantization is only  
71 observable in a large perpendicular magnetic field<sup>24</sup>. These results hint at the presence of various types  
72 of surface disorder that act to suppress the  $E_{g,ex}$ <sup>25</sup> and destroy QAHE.

73  
74 To understand the mechanism of topological breakdown requires direct measurement of the interplay  
75 between surface disorder, local fluctuations in  $E_{g,ex}$ , and the chiral edge state with atomic-scale  
76 precision using low-temperature scanning tunneling microscopy and spectroscopy (STM/STS). A  
77 technique previously used to probe band gap fluctuations and edge states in other 2D materials<sup>2, 18, 28-</sup>  
78 <sup>31</sup>. To date, most STM/STS measurements on  $MnBi_2Te_4$  have been performed on bulk crystals and  
79 have focused on point defects<sup>26, 27, 28</sup>. Little attention has been paid to ultra-thin films of  $MnBi_2Te_4$  and  
80 the mechanisms of topological protection breakdown and suppression of QAHE. A recent report

81 suggests connection between local magnetic  $\text{Mn}_{\text{Bi}}$ ,  $\text{Bi}_{\text{Mn}}$  anti-site defects (notation  $\text{X}_\text{Y}$  means a X ion  
82 replaces a Y ion in the lattice) and collapse of the Dirac mass gap in high defect regions, but did not  
83 measure bandgap fluctuations over large areas to understand possible short-range behavior from  
84 magnetic disorder, how disorder interacts with the chiral edge state<sup>29</sup> or how the disorder effects  
85 respond to a magnetic field. Thus, the mechanism by which topological protection is destroyed, as well  
86 as how it recovers in  $B$  field, are still not understood.

87

88 In this work, we utilize magnetic field STM/STS to study the origin of QAHE suppression in 5 septuple  
89 layer (SL)  $\text{MnBi}_2\text{Te}_4$ . We directly measure spatial fluctuation of  $E_{\text{g,ex}}$  and importantly observe the  
90 electronic overlap of the gapless edge state with gapless metallic bulk states, providing the route to  
91 breakdown of the QAHE. Finally, we demonstrate that by applying a magnetic field well below the  
92 spin-flop transition, we are able to restore the magnetic gap in the gapless regions, explaining the  
93 recovery of QAHE in small magnetic fields.

94

95 **Fig. 1(a)-(b)** presents the crystal structure of one septuple layer (SL)  $\text{MnBi}_2\text{Te}_4$ . Lattice constants,  
96 magnetic moments and possible lattice defects are labelled. Within each SL, intra-layer  $\text{Mn}^{2+}$  ions are  
97 coupled through ferromagnetic interaction. Between two adjacent SLs, two  $\text{Mn}^{2+}$  atomic layers are  
98 coupled through anti-ferromagnetic (AFM) interaction, resulting in thickness-dependent magnetic  
99 properties. We grow high-quality epitaxial ultra-thin  $\text{MnBi}_2\text{Te}_4$  using molecular beam epitaxy (MBE)  
100 on  $\text{Si}(111)\text{-}7\times 7$ . Due to interfacial charge transfer as a result of the different work functions of  $p$ - and  
101  $n$ -type silicon (111) the doping level in  $\text{MnBi}_2\text{Te}_4$  films can be tuned. This allows for STM/STS  
102 measurements performed on  $\text{MnBi}_2\text{Te}_4$  on  $p$ -type  $\text{Si}(111)$  with a Fermi energy that sits in the Dirac  
103 gap, whilst for ARPES measurements performed on  $\text{MnBi}_2\text{Te}_4$  on  $n$ -type  $\text{Si}(111)$  the films are electron-  
104 doped allowing the Dirac electron band to be observed. See Methods for growth details, whilst  
105 structural characterization as well as the role of substrate and doping are found in Supplementary

106 Information **S1 and S2**. Supplementary **Fig. S1(b)** shows a typical large-area STM topography scan  
107 with coexisting regions of 4 and 5 SL  $\text{MnBi}_2\text{Te}_4$  islands that are atomically flat, along with small  
108 pinholes of bare substrate. **Fig. 1(c)** shows a  $20\times 20$  nm atomic resolution STM image revealing the  
109 expected  $1\times 1$  atomic surface structure with lattice constant  $4.3 \text{ \AA}$ . Several different defects are present;  
110 bright spots on the surface correspond to negatively charged  $\text{Bi}_{\text{Te}}$  point defects whilst the dark triangles  
111 are  $\text{Mn}_{\text{Bi}}$  defects, similar defects have been observed in Cr, Mn-doped 3D TIs<sup>19, 30, 31</sup>. The third defect  
112 type –  $\text{Bi}_{\text{Mn}}$  (located in the middle of each SL) is not directly visible in (c) but presented in  
113 **Supplementary Fig. S3**.

114

115 **Fig. 1(d)** shows an ARPES spectrum of 5 SL  $\text{MnBi}_2\text{Te}_4$  thin film grown on *n*-type Si(111) taken at 8  
116 K along  $\Gamma\text{M}$  direction where a Dirac cone is clearly visible near the Fermi level. The strong spectral  
117 weight near  $\Gamma$  in the Dirac point region could be due to Te-orbital-related matrix elements<sup>32, 33</sup> or be  
118 the result of bandgap fluctuations as the spectral signal is averaged over the beam spot size ( $100\times 100$   
119  $\mu\text{m}$ ). To demonstrate this possibility we fit the ARPES spectrum in **Fig. 1(d)** with three possible  
120 scenarios (red curve: full band gap  $E_{\text{g,ex}} = 70 \text{ meV}$  extracted from energy distribution curve analysis<sup>32</sup>,  
121 green curve: reduced  $E_{\text{g,ex}} = 45 \text{ meV}$ , blue curve: gapless  $E_{\text{g,ex}} = 0 \text{ meV}$  limit).

122

123 To properly understand the  $E_{\text{g,ex}}$  distribution, we use STS to measure the  $dI/dV$  spectrum (the  
124 differential conductance  $dI/dV$  as a function of sample bias  $V$ ) which is proportional to the local density  
125 of states (LDOS) at energy  $E_{\text{F}} + eV$ , where  $e$  is the elementary charge. **Fig. 1(e)** shows three typical  
126 STS from the same SL terrace. The size of  $E_{\text{g,ex}}$  changes drastically with location: the red STS curve  
127 corresponds to  $E_{\text{g,ex}} = 70 \text{ meV}$ , the green curve shows a reduced band gap  $E_{\text{g,ex}} = 45 \text{ meV}$ , and the blue  
128 curve is consistent with a gapless ( $E_{\text{g,ex}} = 0 \text{ meV}$ ) spectrum (see **Fig. S4** and **Fig. S5** for details on  
129 extracting bandgap and the minimal tip-induced band bending). All spectra in **Fig. 1(e)** were taken  
130 more than 5 nm away from step edges in order to exclude effects from edge states.

131 Before turning to the origin of the band gap variations, we probe the step edge between 4 and 5 SL  
132  $\text{MnBi}_2\text{Te}_4$ , to verify the presence of the conductive edge state, a consequence of topological protection  
133 and signature of a QAHI. In principle, the edge state exists at the edge of the sample where the height  
134 profile on the sample drops from 5SL thickness to the underlying substrate. However, due to a variety  
135 of growth and measurement practicalities, measuring the edge state on the sample edge with STM is  
136 extremely challenging. Therefore, instead we probe the edge state on the 5SL (Chern number of  $\pm 1$ )  
137 to 4SL (Chern number of 0) step edge enabled by the unique thickness-dependent topological property  
138 of  $\text{MnBi}_2\text{Te}_4$ .<sup>22</sup> Since the edge state appears on the boundary between two phases with different  
139 topological invariant, the physics of the edge state on the terrace edge is equivalent to that of the edge  
140 state on the sample edge.

141

142 **Figure 2(a)** and **(b)** show STM topography and  $dI/dV$  maps taken across two different 4 to 5 SL step  
143 edges on two separately grown  $\text{MnBi}_2\text{Te}_4$  thin films. Since the chiral edge state exists within the  
144 Dirac band gap, the sample bias was tuned into the Dirac band gap to image the edge state. The lower  
145 panel of **Fig. 2(a)** shows a  $dI/dV$  map taken at +25 mV: a pronounced increase in  $dI/dV$  signal is  
146 observed that is localized at the step edge (which is marked by a red dashed line), indicating a  
147 conductive edge state. This conductive edge state is mostly continuous, but has strong hybridization  
148 between the edge state and disordered bulk states and not spatially isolated. The second edge  
149 presented in **Fig. 2(b)** shows another step edge consisting a 5SL edge (orange arrow) and sub-step  
150 edge (excluded in the figure). The sub-step edge structure has also been observed in previous STM  
151 study on  $\text{MnBi}_2\text{Te}_4$  thin films<sup>29</sup>. The middle and lower panel of **Fig. 2(b)** show  $dI/dV$  maps taken  
152 at 0 and -15 mV: that also show a pronounced increase in  $dI/dV$  signal that is localized at the step  
153 edge. At bias outside the Dirac gap (-15 mV), this edge state is weakly coupled to bulk state with  
154 finite spectral weight between the edge channel and the gapless bulk states. As the bias moves into the  
155 Dirac gap (0 mV), the edge states become spatially isolated unlike the edge state presented in **Fig.**  
**2(a)**. We have included more  $dI/dV$

156 maps at other voltage bias, see **Fig.S6** to demonstrate the decoupled edge channel in the Dirac gap.  
157 We must point out the spectral intensity along the edge in **Fig. 2(b)** seems to be disconnected, which  
158 has been also observed in previous reports on topological edge states of  $\text{MnBi}_2\text{Te}_4$ <sup>34</sup>, its related  
159 heterostructure with  $\text{Bi}_2\text{Te}_3$ <sup>35</sup>, as well as the 2D topological insulator  $\text{WTe}_2$ <sup>36</sup> and may arise due to  
160 local roughness and structural disorder along the edge. Furthermore, we have also performed a similar  
161  $dI/dV$  map on a 4SL to 3SL edge, and no spectral intensity is observed (**Fig.S7**), indicating the 1D  
162 edge state could be only present on odd-layer SL  $\text{MnBi}_2\text{Te}_4$  that is buried underneath the step edge and  
163 is very difficult to probe from the surface. For a perfect QAHI there should be a well-defined  
164 suppression of the bulk LDOS within the bandgap, but we observe bulk regions well away from the  
165 edge that also show strong LDOS at the same energy, indicating the coupling between edge state and  
166 disordered bulk metallic regions. To confirm that some disordered bulk regions are indeed metallic, in  
167 **Fig. 2(c)** we measure  $dI/dV$  spectra corresponding to the edge state (red curve) at point A, normal bulk  
168 states (purple curve) at point B, and disordered bulk states (black curve) at point C, D in **Fig. 2(b)**. The  
169 normal bulk region right next to the edge shows the expected insulating behavior with  $E_{g,\text{ex}} = 40$  meV,  
170 but the  $dI/dV$  spectra at both the edge and within these disordered bulk state regions are quite different,  
171 with states filling the entire bulk gap. The disordered bulk states have much stronger spectral intensity  
172 above zero bias in the conduction band range and the STS curves resembles the DOS of a gapless  
173 Dirac cone<sup>37</sup>. This indicates a continuous metallic percolative path for electron transport from the edges  
174 through the bulk. **Figure 2(d), (e)** shows spatial  $dI/dV$  profiles as a function of distance away from the  
175 edge measured along the two green lines in **Fig. 2(b)** (labelled as Cut 1 and Cut 2) that demonstrate  
176 the extended nature of the edge state feature along the step edge located at 5 nm, as marked by the red  
177 arrow. The other spectral intensity between 0 to 2 nm is clearly separated from the edge state, and we  
178 assign it to the disordered bulk states, marked by a white arrow. **Figure 2(f)** shows the summed  $dI/dV$   
179 intensity (red curve extracted from **Fig. 2(d)**; green curve extracted from **Fig. 2(e)**) within the bulk  
180 Dirac gap. Moving away from the edge shows the expected exponential decay for a 1D topologically



181 non-trivial edge state. <sup>2,38</sup>The extracted exponential decay lengths are  $0.82 \pm 0.38$  nm and  $1.22 \pm 0.41$   
182 nm. Although the observed edge state appears to be isolated from the metallic bulk states, the small  
183 spatial separation (less than 3 nm) implies fragile edge state conduction. The observation of a 1D edge  
184 state on two different step edges (**Fig. 2** and additional data presented in **Fig. S8**), suggests the 1D  
185 edge state exists on the 5SL to 4SL edge, independent of the exact edge structure and evidence of a  
186 QAH gapless edge state. However, the presence of both disordered bulk state and edge state on the  
187 5SL terrace suggests that the edge state hybridizes with the metallic regions formed by these disordered  
188 bulk states, and these metallic regions represent continuous conductive pathways that guide the edge  
189 state into the bulk, leading to the conductive breakdown of QAHE through dissipative bulk conduction  
190 and resulting in non-perfect quantization of Hall conductance and non-zero longitudinal resistance.

191

192 To investigate the origin of these metallic regions formed by disordered bulk states, we perform atomic  
193 resolution topography and STS maps around the magnetic defects  $\text{Mn}_{\text{Bi}}$  and  $\text{Bi}_{\text{Mn}}$ , which allow us to  
194 extract maps of the spatial variation of  $E_{\text{g,ex}}$ , and the gap center energy  $E_c$  to determine the influence  
195 each defect has on the electronic structure.  $E_c$  is equivalent to extrapolating the massive Dirac bands  
196 linearly into the gap to obtain the Dirac point in the gapless limit. At locations where the Dirac bands  
197 are gapped,  $E_c$  is a good measure of local doping shifts associated to the magnetic order.  $\text{Bi}_{\text{Te}}$  defects,  
198 are non-magnetic, thus, are unlikely to result in fluctuations in the exchange energy gap  $E_{\text{g,ex}}$ . **Figure**  
199 **3(a)** illustrates the position of a  $\text{Mn}_{\text{Bi}}$  defect in the crystal lattice, and **Fig. 3(b)** shows an atomic  
200 resolution image of  $10 \times 5$  nm area (-500 mV, 3 nA) with  $\text{Mn}_{\text{Bi}}$  defects marked in black triangles. The  
201  $\text{Mn}_{\text{Bi}}$  defect density can be estimated to be around 6%, which is very similar to the defect concentration  
202 reported in previous study on MBE grown  $\text{MnBi}_2\text{Te}_4$  film<sup>29</sup> but is almost double the concentration  
203 observed on the surface of a cleaved bulk  $\text{MnBi}_2\text{Te}_4$  crystal<sup>27</sup>. The substitution of  $\text{Bi}^{3+}$  by  $\text{Mn}^{2+}$  causes  
204 contraction on the three neighboring surface Te atoms<sup>27</sup>. **Fig. 3(c)-(d)** are maps of  $E_{\text{g,ex}}$  and  $E_c$  extracted  
205 from the  $dI/dV$  spectra on the same area in (b) (details found in **Supplementary Fig. S4**).

206 Representative  $dI/dV$  curves from different locations, marked with  $E_{g,ex}$  and  $E_c$  values, are plotted in  
207 **Supplementary Fig. S9**. The Mn<sub>Bi</sub> defects on the surface (green triangles) are barely visible in the  
208 maps of  $E_{g,ex}$  and  $E_c$  in (c) and (d) respectively, with only small local decrease in  $E_{g,ex}$  and slight  
209 increase in  $n$ -type doping (due to the negative charge of the Mn<sub>Bi</sub> defects) observed. Instead, the  
210 fluctuations in  $E_{g,ex}$  and  $E_c$  appear to be correlated, and to be spatially coherent over length scales of at  
211 least a few nanometers, i.e. larger than a single defect which is about 0.5 nm. Gap size histograms of Mn<sub>Bi</sub>  
212 regions and Mn<sub>Bi</sub> excluded regions are shown in **Fig. 3(e)**. In regions without Mn<sub>Bi</sub> defects, the  $E_{g,ex}$   
213 histogram is skewed towards larger gap size when compared to regions with Mn<sub>Bi</sub> defects, which can  
214 be explained by effectively reduced exchange coupling between surface state and magnetic moments  
215 due to the AFM interaction between the Mn<sub>Bi</sub> defects and Mn<sup>2+</sup> ions. Overall, the patterns of gapped and  
216 gapless regions formed over several nanometers are very different from the band gap fluctuations in  
217 dilute magnetic doped TIs<sup>19,31</sup>. In dilute magnetic doped TIs, the random distribution of antisites formed by  
218 magnetic 3d transition metal ions is directly responsible for the fluctuation. But in the current case of 5SL  
219 MnBi<sub>2</sub>Te<sub>4</sub> thin film, the observed pattern in the  $E_{g,ex}$  map appears to be not correlated to distribution of Mn<sub>Bi</sub>  
220 defects, suggesting additional major contribution from magnetic disorder to the gap fluctuations. The  
221 origin of the magnetic disorder can be complicated but is very likely to be defect driven. The local  
222 deficiency of Bi  $p$ -states on Mn<sub>Bi</sub> defects could indirectly modulate the weakened intralayer ferromagnetic  
223 interaction among Mn<sup>2+</sup> magnetic moments through non-negligible  $p$ - $d$  interactions, as reported by  
224 recent magneto-optics and inelastic neutron scattering studies<sup>39,40</sup>. In **Fig. 3(f)**, a Bi<sub>Mn</sub> defect in the  
225 middle atomic layer is depicted, where the substitution results in the absence of magnetic moment. Such  
226 defects manifest as large bright triangles and are only visible at positive bias as marked by purple triangles  
227 in (g). The three bright dots in each triangle are due to Te  $p$ -orbitals on the surface responding to Bi<sub>Mn</sub>  
228 defects<sup>27</sup>.  $dI/dV$  mapping was performed in the area marked by the yellow box in (g), with the band gap  
229 and gap center maps shown in **Fig. 3(h)-(i)**. The band gap map in (h) and the histogram in (j) show that the  
230 substitution of magnetic Mn<sup>2+</sup> ions at

231  $\text{Bi}_{\text{Mn}}$  defects renders the local lattice site non-magnetic, thus, gapless regions. However, regions well  
232 away from the  $\text{Bi}_{\text{Mn}}$  defect still display band gap fluctuation with significant weight of gapless states,  
233 suggesting that  $\text{Bi}_{\text{Mn}}$  defects alone do not result in extended regions of suppressed Dirac band gap and  
234 metallicity in the bulk. The results in **Fig. 3** therefore demonstrate the band gap and gap center  
235 fluctuations cannot be explained entirely by local gap suppression by any of the three types of isolated  
236 point defects discussed above and imply the possibility that longer-ranged collective behavior of  
237 magnetic disorder is responsible for the extended Dirac band gap suppression on the surface of  
238  $\text{MnBi}_2\text{Te}_4$ .

239

240 To understand the origin of the observed large-scale band gap fluctuations, we measure STS mapping  
241 with and without magnetic field to examine how the extended gapless structures respond to  $B_{\perp}$  field.

242 **Figure 4(a)** shows STM topography of the atomically flat scan region at  $B_{\perp}=0$  T. (See **Fig.S10** for the  
243 topography scan taken at 0T and 1T where the map region has been carefully aligned using the defects).

244 In **Fig. 4(b)** STS curves taken at different locations show three types of behavior: gapless regions  
245 (blue), gapped regions with fluctuating Dirac band gap (green and red) and regions where the Dirac  
246 electron band is suppressed and manifests as an anomalously large bulk gap (orange). Such conduction  
247 band (CB) suppression has been previously observed in bulk  $\text{MnBi}_2\text{Te}_4$ <sup>27</sup>. The diminished CB intensity

248 prevents us from extracting accurate values of  $E_{\text{g,ex}}$ , thus, the CB suppressed regions are masked in  
249 black in the following gap maps and excluded in subsequent analysis. The CB suppressed regions are

250 identified by summing the STS intensity above +20 mV bias at each point and comparing to a summed  
251 threshold value of  $1.28 \times 10^{-11}$  for 0 T map and  $1.85 \times 10^{-11}$  for 1T map that are estimated from STS

252 curves with weak CB intensity and optimized. **Figure 4(d)** plots STS curves taken at the same location  
253 (green circle in **(a)**) that is initially gapless at  $B_{\perp}=0$  T (blue curve) and  $B_{\perp}=1$  T (red curve). It is

254 immediately clear that a 1 T field is sufficient to restore  $E_{\text{g,ex}}$  to 40 meV with enhanced exchange  
255 coupling. Having observed magnetic field induced band gap modulation, we now perform  $dI/dV$

256 mapping (-150 mV, 0.4 nA) on an 80×80 point-mesh on the same 30×30 nm area in (a) at  $B_{\perp}=0$  T  
257 (Fig. 4(c)) and  $B_{\perp}=1$  T (Fig. 4(e)). Histograms of  $E_{g,ex}$  with and without  $B$  field are shown in Fig. 4(f).  
258 These maps reflect the spatial fluctuation of  $E_{g,ex}$  over larger scale and will be used to investigate its  
259 origin beyond point defects. The histogram in the upper panel of Fig. 4(f), shows prominent weighting  
260 for  $E_{g,ex} < 10$  meV, corresponding to a skewed normal distribution (skewness 0.91) with mean of 26.3  
261 meV and standard deviation of 25.8 meV. Upon applying  $B_{\perp}=1$  T, the histogram in the lower panel of  
262 Fig. 4(f) shows a significant reduction in  $E_{g,ex} < 10$  meV regions, and a gap opening and  
263 renormalization that results in a near-normal distribution (skewness 0.06) with an increased mean of  
264 44.3 meV and smaller standard deviation of 20.2 meV. A statistical analysis of regions that possess  
265 unsuppressed CB intensity at both 0T and 1T is presented in the Supplementary Information in Fig.  
266 S11. This shows the average band gap increases by 20.6 meV to a value of 37.8 meV in the 1T  
267 magnetic field and more bimodal distribution. Additionally, to reveal the gradual change of the  $E_{g,ex}$   
268 in low to medium magnetic field, we have performed magnetic field dependent mapping between 0  
269 and 0.8 T on a different sample, see Fig. S12 where the majority of gap renormalization occurs at 0.8  
270 T.

271

272 We now consider possible origins of the extended suppressed gap structures. As recently observed in  
273 magnetic force microscopy measurements<sup>41</sup>, whilst the bulk of MnBi<sub>2</sub>Te<sub>4</sub> thin film remains AFM  
274 coupled, the surface exhibits magnetic spin flops which could be enhanced by Bi<sub>1-x</sub>Mn<sub>x</sub> defects or changes  
275 to the size of the inter-layer van der Waals gap near the surface<sup>42</sup>. In our thin film MnBi<sub>2</sub>Te<sub>4</sub> samples,  
276 we are able to align the magnetic moments at  $B_{\perp}=1$  T, much lower than required for inducing surface  
277 (2-3.5 T) and bulk spin flop (7.7 T) in previous work<sup>41,43,44</sup>, which indicates that surface spin flop has  
278 negligible contribution to the exchange gap fluctuation observed. This suggests that there is significant  
279 magnetic disorder most likely in the first SL, a magnetic uncompensated layer, that causes band gap  
280 fluctuation on the nanometer scale<sup>25</sup>. Such magnetic disorder occurs in the Mn<sup>2+</sup> layer located at the

281 center of the top SLs, which is very hard to probe using STM. However, the exchange interaction of  
282 the Dirac states with  $\text{Mn}^{2+}$  ions enables indirect mapping of such magnetic disorder based on the  
283 suppression of  $E_{\text{g,ex}}$  as seen in **Fig. 4(c)** and **(e)**.

284

285 **Fig. 4(g)** illustrates the situation schematically. Magnetic disorder causes local suppression of the  
286 exchange gap (blue gapless Dirac spectrum) in extended regions due to long-range exchange  
287 interactions among local moments, while some regions retain partial (green band structure) or full (red  
288 band structure) gaps. Application of  $B_{\perp}=1\text{T}$  (bottom) aligns the moments of magnetically disordered  
289 regions, increasing the gap (red band structure). Interestingly, the  $B$  field also decreases the area of  
290 suppressed CB regions, suggesting CB suppression is also related to disordered magnetic moments  
291 beyond the influence of deficient Bi orbitals due to  $\text{Mn}_{\text{Bi}}$  defects<sup>27</sup>. Finally, we propose an explanation  
292 to the origin of the magnetic disorder. The prevalent band gap fluctuation observed implies weakened  
293 inter-layer and intra-layer exchange interaction in 5 SL  $\text{MnBi}_2\text{Te}_4$ . Its low magnetic anisotropy energy  
294 makes  $\text{MnBi}_2\text{Te}_4$  similar to a 2D Heisenberg magnet that does not sustain long-range ferromagnetic  
295 order<sup>40, 44, 45</sup>. Such weakened magnetic anisotropy makes the magnetic ordering more vulnerable to  
296 magnetic defects, especially  $\text{Bi}_{\text{Mn}}$ . With  $\text{Mn}^{2+}$  ions replaced by non-magnetic  $\text{Bi}^{3+}$  ions, exchange  
297 coupling between intra-layer  $\text{Mn}^{2+}$  ions is weakened, depending on the concentration of such defects.  
298 Although, the direct exchange coupling between  $\text{Mn}_{\text{Bi}}$  and surface states is much weaker as discussed  
299 in **Fig. 3**,  $\text{Mn}_{\text{Bi}}$  can still cause local deficiency of Bi  $p$ -orbitals and indirectly influence the magnetic  
300 moments in the middle of SL by  $p$ - $d$  interaction. Therefore, the ferromagnetic configuration of  $\text{Mn}^{2+}$   
301 ions could be canted and disordered in the presence of a large amount of anti-sites defects, resulting in  
302 reduced magnetization and gapless spectra over extended areas. Similar mechanism has also been  
303 reported recently<sup>29</sup>. Lastly, we present an  $E_{\text{g,ex}}$  map of a region with larger amount of  $\text{Bi}_{\text{Mn}}$  defects in  
304 0 T and 1 T magnetic field in **Fig. S13**. This region is indeed mostly gapless. Upon applying the 1T  
305 field, a significant reduction of gapless regions occurs (further details in **Supplementary Fig. S13**).

306 CB suppression is almost absent in this region, which can be explained by the large amount of  $\text{Bi}_{\text{Mn}}$   
307 defects that offers sufficient  $p$ -states to form Dirac bands.  
308  
309 Using magnetic field STM/STS measurements, we have demonstrated that the gapless edge state in  
310 QAHE 5 SL  $\text{MnBi}_2\text{Te}_4$  is directly coupled to extended percolating bulk metallic regions arising from  
311 band gap fluctuations caused by magnetic surface disorder. By applying a magnetic field, the band gap  
312 fluctuations can be greatly reduced, and the average exchange gap increased to 44 meV, close to  
313 predicted values for 5 SL  $\text{MnBi}_2\text{Te}_4$ <sup>21,22, 32</sup>. These results provide insight on the mechanism of  
314 topological breakdown and how it can be restored in a magnetic field<sup>23,24</sup>. Minimizing magnetic  
315 disorder will be the key to realizing QAHE in not only odd-layer  $\text{MnBi}_2\text{Te}_4$  ultra-thin films but also  
316 other MTIs at elevated temperature in the future. The weak interlayer interaction and intralayer  
317 ferromagnetic ground state close to instability limit in  $\text{MnBi}_2\text{Te}_4$  makes it difficult to sustain long-  
318 range magnetic order especially with significant amount of anti-site defects, and improved  $\text{MnBi}_2\text{Te}_4$   
319 crystal or film growth alone may not be sufficient to fully mitigate magnetic disorder. Therefore, other  
320 strategies such as heterostructure engineering  $\text{MnBi}_2\text{Te}_4$  with other robust, highly anisotropic 2D  
321 ferromagnets<sup>46</sup> or ferromagnetic/topological insulators sandwich heterostructures<sup>47, 48, 49</sup> may be  
322 required to achieve the robust topological protection required for next-generation lossless electronics  
323 and topological quantum computing<sup>6,7,8,9</sup>.

324

## 325 Methods

### 326 Growth of Ultra-thin $\text{MnBi}_2\text{Te}_4$ on Si(111)

327 Ultra-thin  $\text{MnBi}_2\text{Te}_4$  thin films were grown in a Scienta Omicron Lab 10 molecular beam epitaxy  
328 (MBE) growth chamber. The Si(111) substrate was flash-annealed at 1180°C with direct current  
329 heating to achieve an atomically flat (7×7) surface reconstruction. Effusion cells were used to  
330 evaporate elemental Mn (99.9%), Bi (99.999%) and Te (99.95%). A quartz crystal microbalance was  
331 used to calibrate rates before growth and reflection high-energy electron diffraction (RHEED) was  
332 used to monitor the crystal growth in-situ. Each SL of  $\text{MnBi}_2\text{Te}_4$  was grown by first growing 1  
333 quintuple-layer  $\text{Bi}_2\text{Te}_3$  followed by growing a bilayer MnTe in overflux of Te at 230 °C. 1 SL  
334  $\text{MnBi}_2\text{Te}_4$  forms spontaneously by re-arranging MnTe layer into the middle of 1QL  $\text{Bi}_2\text{Te}_3$  similar to  
335  $\text{MnBi}_2\text{Se}_4$ <sup>50</sup>. The growth time for each 1QL  $\text{Bi}_2\text{Te}_3$  and MnTe was calibrated from the oscillation of  
336 the RHEED pattern. Then the process was repeated five times to reach the desired thickness and

337 finished with a post-annealing process in Te flux for 10 min to improve crystallinity. The films were  
338 subsequently capped with 10nm amorphous Te, to allow transfer in air to the STM chamber.  
339

### 340 **Scanning Tunneling Microscopy/Spectroscopy (STM/STS) Measurements**

341 The capped films grown on boron doped silicon (111) (resistivity 0.1-0.2  $\Omega \cdot \text{cm}$ ) were transferred in  
342 air to a Createc LT-STM chamber and were annealed in UHV at 290°C for 2.5 hours to remove the Te  
343 capping before performing STM measurements at 4.3 K. A PtIr tip was prepared and calibrated using  
344 an Au (111) single crystal, confirming the presence of the Shockley surface state at -0.5 V and flat  
345 LDOS near the Fermi level before all measurements. The STM differential conductance measurements  
346 ( $dI/dV$ ) were performed using standard lock-in method with 5 mV AC excitation voltage at 797Hz for  
347 Dirac gap mapping and 2mV AC excitation voltage at 797Hz for edge state mapping. Differential  
348 conductance measurements were made under open feedback conditions with the tip in a fixed position  
349 above the surface. For the magnetic field dependent STM/STS measurements, a magnetic field up to  
350 1T was applied perpendicular to the sample.  
351

### 352 **Angle-resolved Photoemission Spectroscopy (ARPES) Measurements**

353 ARPES measurements were performed at Beamline 10.0.1 at Advanced Light Source (ALS) in  
354 Lawrence Berkeley National Laboratory, USA. A 5 SL  $\text{MnBi}_2\text{Te}_4$  sample was grown on antimony  
355 doped silicon (111) substrate (resistivity 0.1-0.2  $\Omega \cdot \text{cm}$ ) following the same growth procedure in an  
356 MBE system integrated with the beamline endstation and transferred into the measurement chamber  
357 after growth. Data was taken using a Scienta R4000 analyser at 8K and photon energy of 50 eV was  
358 selected to optimize the signal. The combined energy resolution is 15-20 meV and the angular  
359 resolution is 0.2°, or equivalent to 0.01 $\text{\AA}^{-1}$  momentum resolution for the photon energy used.  
360

### 361 **Acknowledgements**

362 M. T. E., Q. L., M. S. F., I. D. B. acknowledge funding support from ARC Centre for Future Low  
363 Energy Electronics Technologies (FLEET) CE170100039. Q. Li acknowledges funding support from  
364 the AINSE postgraduate award. This research used resources of the Advanced Light Source, which is  
365 a DOE Office and Science User Facility under contract no. DE-AC02-05CH11231. M.T.E. and Q.L.  
366 acknowledge travel funding provided by the International Synchrotron Access Program (ISAP)  
367 managed by the Australian Synchrotron, part of ANSTO, and funded by the Australian Government.  
368 This work was performed in part at the Melbourne Centre for Nanofabrication (MCN), the Victorian  
369 Node of the Australian National Fabrication Facility (ANFF).  
370

### 371 **Author contributions**

372 M. T. E and Q. L. devised the STM experiments. Q. L. performed the MBE growth and STM/STS  
373 measurements at Monash University. I. D. B., B. L., L. W. and T.H.Y.V assisted the scanning probe  
374 measurements. J. H., S.-K. M. and C. X. T assisted the ARPES measurements. Q. L. performed data  
375 analysis with assistance from M. T. E, M. S. F, J. M and D. M. Q. Li, and M. T. E. composed the  
376 manuscript. All authors read and contributed feedback to the manuscript.  
377

### 378 **Data availability**

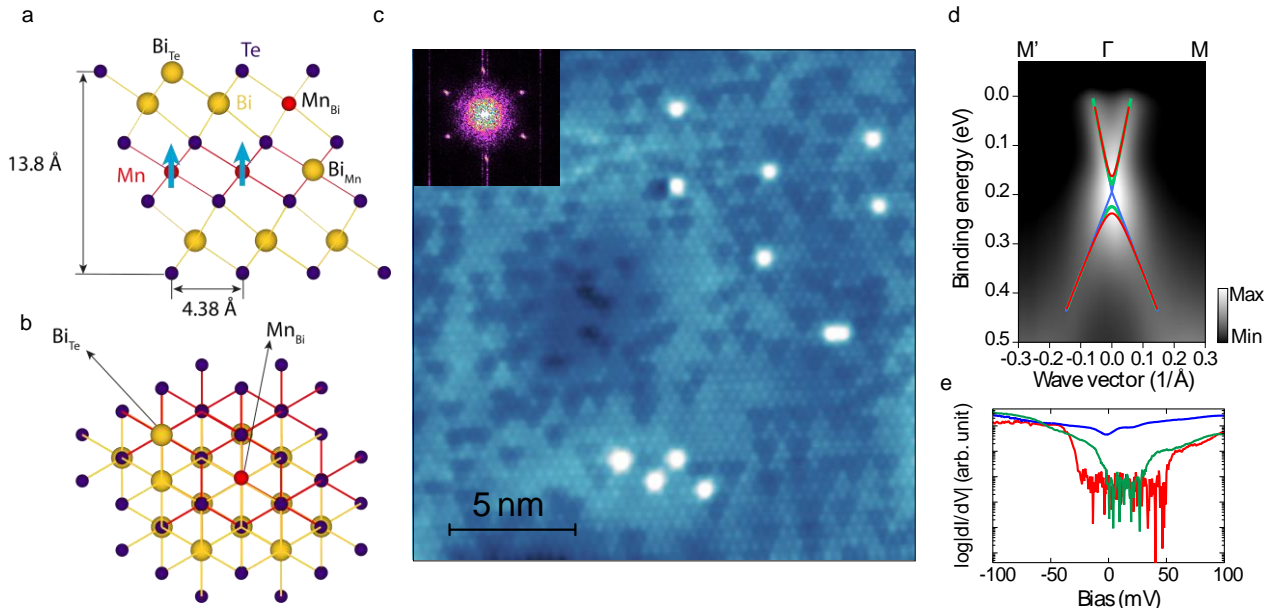
379 All raw and derived data used to support the findings of this work are available from the authors on  
380 reasonable request.

381 **FIGURES**

382

383 **FIGURE 1**

384



385

386

387

388

389

390

391

392

393

394

395

396

397

398

399

400

401

402

403

404

405

406

407

408

409

410

411

412

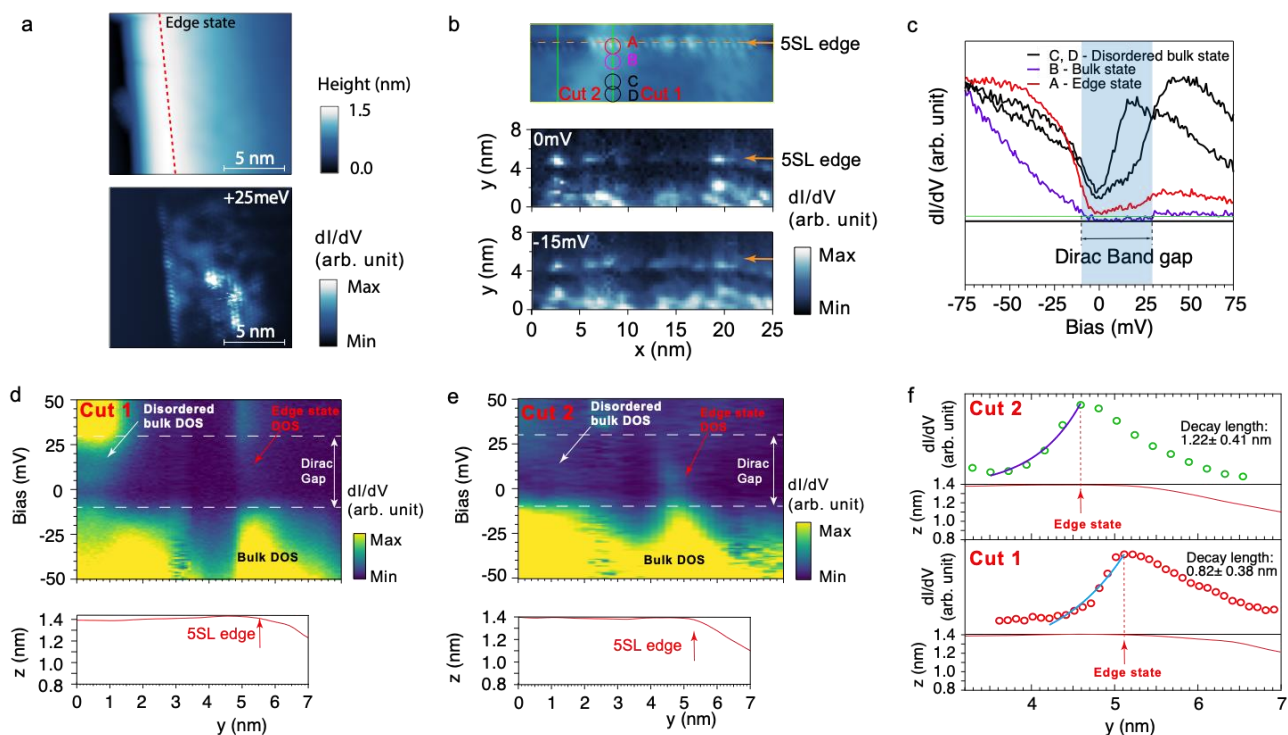
413

414

415

**Figure 1 | Characterization of epitaxial ultra-thin MnBi<sub>2</sub>Te<sub>4</sub> and overall electronic structure from ARPES. (a, b)** Crystal structures of a septuple layer of MnBi<sub>2</sub>Te<sub>4</sub>. **(a)** side view of the lattice with lattice constants, atom species, and defects labelled. The magnetic moments on Mn<sup>2+</sup> ions are marked with blue arrows. **(b)** Top view of the lattice. **(c)** Atomic resolution image (-2 V, 180 pA) of a flat 20×20 nm area where Mn<sub>Bi</sub> (dark triangles) and Bi<sub>Te</sub> (bright dots) defects are clearly visible. The insert shows the fast Fourier transformed image of the same area. (Note the spots corresponding to 1×1 surface atomic structure). **(d)** Angle-resolved photoemission spectrum of five-layer MnBi<sub>2</sub>Te<sub>4</sub> along Γ-M where the fully gapped ( $E_{g,ex} = 70$  meV) band dispersion is marked by red curve. Green and blue are illustrations of possible reduced gap and gapless dispersions ( $E_{g,ex} = 35$  meV and 0 meV respectively). **(e)** dI/dV spectra taken at different locations on the same terrace of 5 SL MnBi<sub>2</sub>Te<sub>4</sub> (-0.2 V, 400 pA) showing gapless (blue curve), reduced gap (green curve) and fully gapped dI/dV curves from different regions on the same terrace.

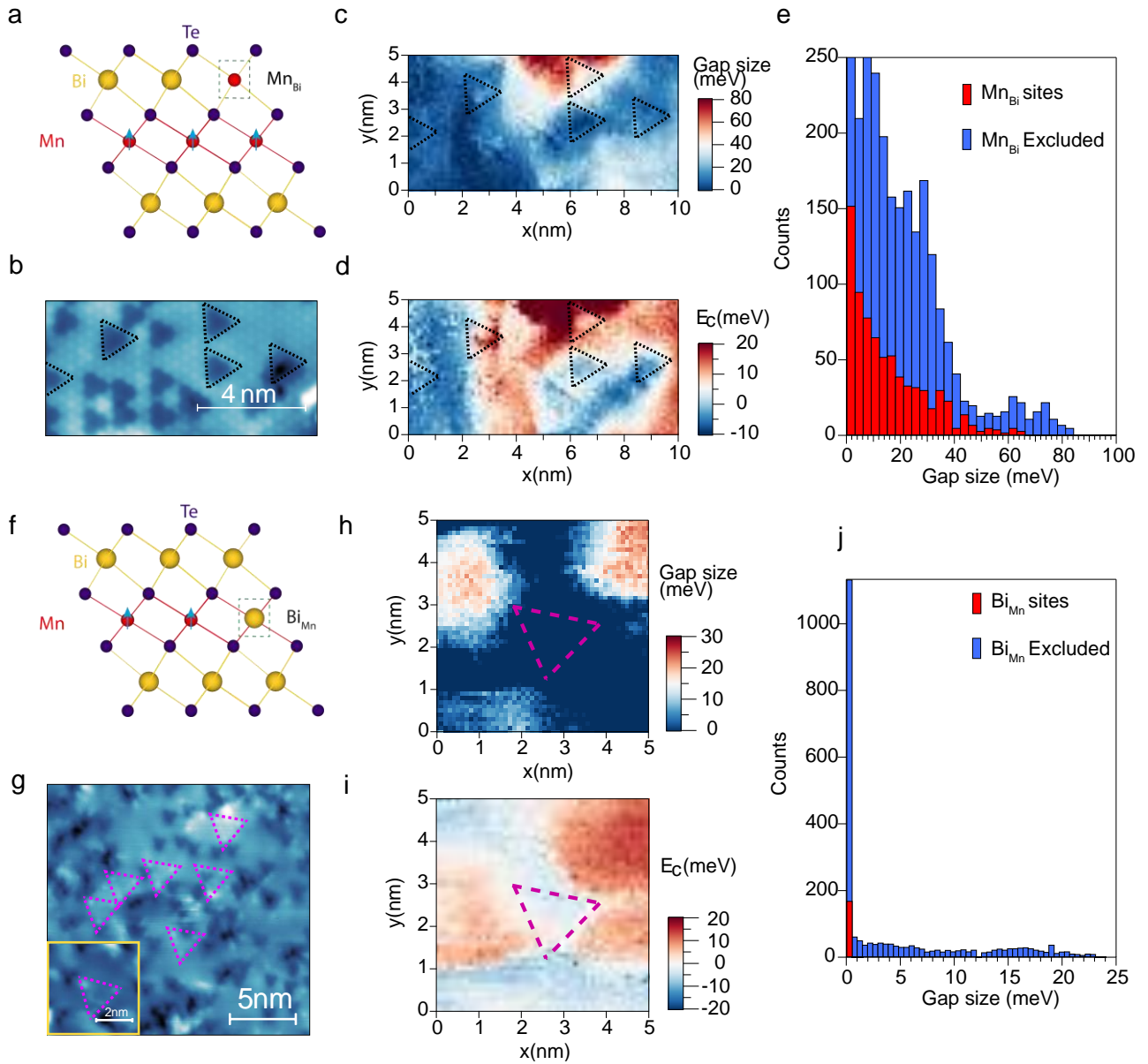




417  
 418 **Figure 2 | Visualizing the gapless edge state and its coupling to bulk metallic states.** (a)-(b) STM  
 419 topography taken at -1V (upper panels) and  $dI/dV$  maps (lower panels) taken across two different 4  
 420 to 5 SL MnBi<sub>2</sub>Te 4step edges. (a)  $dI/dV$  map at +25 mV bias (40 pA) shows a pronounced increase  
 421 in intensity at the edge state and its strong coupling to bulk metallic states. The location of the edge  
 422 state is marked by a red dashed line. (b)  $dI/dV$  maps (-0.15V, 400pA) at 0 mV and -15 mV bias show  
 423 the spatial distribution of the edge state taken across a step edge and how the edge state is isolated  
 424 from the bulk metallic states. The positions of the 5SL edge is marked with orange arrows. (c)  $dI/dV$   
 425 spectra (-0.15V, 400pA) taken from edge state region A (red circle), disordered bulk region C, D (black  
 426 circle) and normal bulk region B (purple circle) as marked in (b). (d),(e)  $dI/dV$  spectra (-0.15V,  
 427 400pA) and height profile taken across the edge from paths marked by green lines in (b). The  
 428 horizontal axis of the spectra is aligned with the height profile. The edge state is marked by red  
 429 arrow and other in-gap peaks are attributed to disordered bulk states which is marked by white  
 430 arrows. The white horizontal dashed line shows the range of Dirac gap which is the same as the  
 431 shaded region in (c). (f)  $dI/dV$  intensity averaged in the Dirac gap and plotted as a function of  
 432 distance in y direction showing exponential decay. The height profiles of the two cuts are shown  
 433 below the  $dI/dV$  profiles respectively where the intensity maximum of the edge state is marked.  
 434  
 435  
 436  
 437  
 438  
 439  
 440  
 441  
 442  
 443  
 444  
 445  
 446

447  
448  
449  
450

FIGURE 3

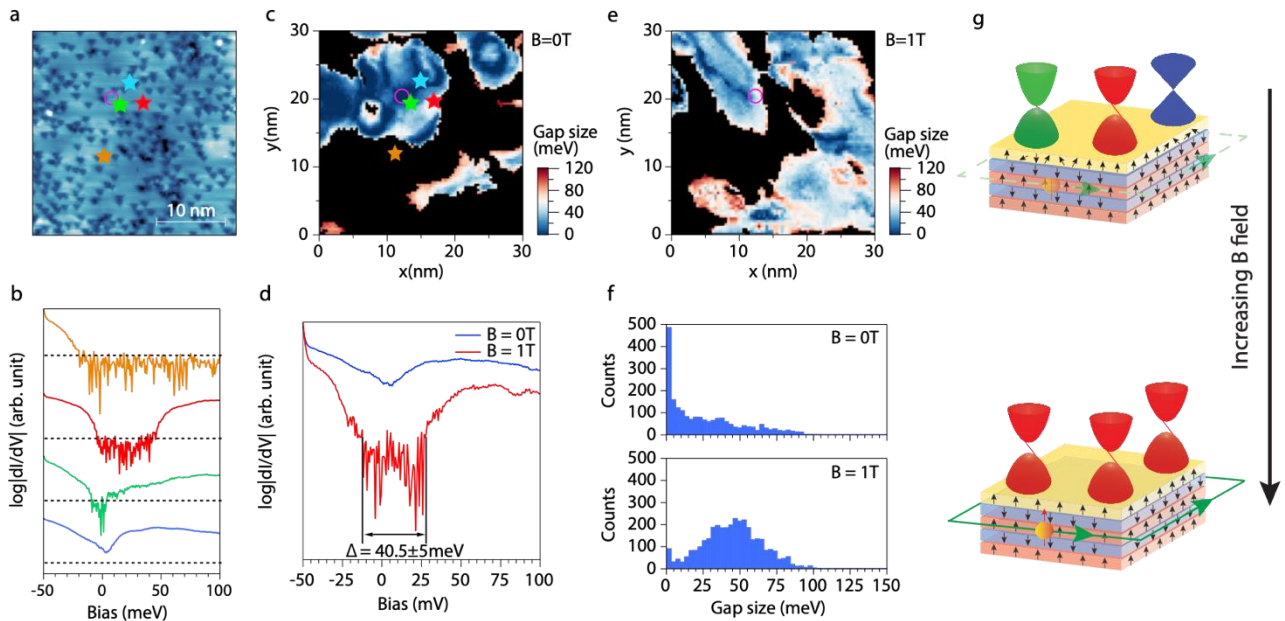


451  
452  
453  
454  
455  
456  
457  
458  
459  
460  
461  
462  
463  
464

**Figure 3 | Local response of the exchange gap and doping to point defects.** (a) Illustration of a Mn<sub>Bi</sub> defect in the lattice. (b) Topography of a 10×5 nm area (-150 mV, 3 nA) with Mn<sub>Bi</sub> defects manifesting as dark triangles (marked in black triangles). (c) An exchange gap,  $E_{g,ex}$ , map extracted from  $dI/dV$  spectra (-100 mV, 0.8 nA) on a 40×80 mesh for visualizing band gap fluctuation and (d) gap center from the same region as (c). (e) Histograms of the  $E_{g,ex}$  extracted from regions with and without Mn<sub>Bi</sub> defects respectively. (f) Illustration of a Bi<sub>Mn</sub> defect in the lattice. (g) Topography of a 40×40 nm area (+1.7 eV, 80 pA) with Bi<sub>Mn</sub> defects which manifest as bigger bright triangles (marked as purple triangles). Insert: a 5×5 nm region where  $dI/dV$  spectra (-100 mV, 0.91 nA) on a 50×50 mesh was taken to show its effect on  $E_{g,ex}$  (h) and doping level which is reflected on gap center (i). (j) Histograms of  $E_{g,ex}$  extracted from the defect region and region excluding the defect.

465  
466  
467  
468

FIGURE 4



469  
470  
471  
472  
473  
474  
475  
476  
477  
478  
479  
480  
481  
482  
483  
484  
485  
486  
487  
488  
489  
490  
491  
492  
493  
494  
495  
496

**Figure 4 | Magnetic field-induced modulation of the exchange gap.** (a) Topography scan (-0.5 V, 100 pA) of a 30×30 nm area where magnetic field dependent STS measurements were conducted. (b) Representative  $dI/dV$  spectra taken at different locations, blue: gapless regions, green: reduced-gap regions, red: large-gap regions and orange: regions where Dirac electron band is suppressed which prevents us from extracting the band gap. (c) Band gap map (80×80 points, -150 mV, 400 pA) of the region in (a) at magnetic field  $B = 0$  T. (d)  $dI/dV$  spectrum taken at the position marked by purple circle in (a) at  $B = 0$  T (blue) and  $B = 1$  T (red). A magnetic Dirac gap of 40.5 meV is opened with 1 T field in a gapless region at 0 T. (e) Band gap map (80×80 points, -150 mV, 400 pA) of the same region in (a) at  $B = 1$  T. Black regions in (c) and (e) correspond to the suppressed Dirac electron band regions which prevent accurate determination of the exchange gap and are excluded from the maps and subsequent histograms in (f). (f) Histograms showing gap size at  $B = 0$  T (upper panel) and  $B = 1$  T (lower panel). A clear renormalization of bandgap is observed with magnetic field. (g) Illustration of the band gap spatial fluctuation caused by surface magnetic disorder which can be reduced significantly by applying a perpendicular magnetic field. The blue, green and red Dirac cones represent gapless, partially gapped and fully gapped regions. Their representative  $dI/dV$  curves can be found in **Figure 1(f)**. Upon applying a perpendicular magnetic field, the exchange gap in the Dirac cones increases until it reaches saturation.

497

498

## 499 References

500

- 501 1. Schindler F, Wang Z, Vergniory MG, Cook AM, Murani A, Sengupta S, *et al.* Higher-order  
502 topology in bismuth. *Nature Physics* 2018, **14**(9): 918-924.
- 503
- 504 2. Reis F, Li G, Dudy L, Bauernfeind M, Glass S, Hanke W, *et al.* Bismuthene on a SiC substrate: A  
505 candidate for a high-temperature quantum spin Hall material. *Science* 2017, **357**(6348): 287-  
506 290.
- 507
- 508 3. Tanaka Y, Ren Z, Sato T, Nakayama K, Souma S, Takahashi T, *et al.* Experimental realization of  
509 a topological crystalline insulator in SnTe. *Nature Physics* 2012, **8**(11): 800-803.
- 510
- 511 4. Liu C, Wang Y, Li H, Wu Y, Li Y, Li J, *et al.* Robust axion insulator and Chern insulator phases in  
512 a two-dimensional antiferromagnetic topological insulator. *Nature Materials* 2020, **19**(5):  
513 522-527.
- 514
- 515 5. Hasan MZ, Kane CL. Colloquium: Topological insulators. *Reviews of Modern Physics* 2010,  
516 **82**(4): 3045-3067.
- 517
- 518 6. Bestwick AJ, Fox EJ, Kou X, Pan L, Wang KL, Goldhaber-Gordon D. Precise Quantization of the  
519 Anomalous Hall Effect near Zero Magnetic Field. *Physical Review Letters* 2015, **114**(18):  
520 187201.
- 521
- 522 7. Chang C-Z, Zhao W, Kim DY, Zhang H, Assaf BA, Heiman D, *et al.* High-precision realization of  
523 robust quantum anomalous Hall state in a hard ferromagnetic topological insulator. *Nature*  
524 *Materials* 2015, **14**(5): 473-477.
- 525
- 526 8. Lian B, Sun X-Q, Vaezi A, Qi X-L, Zhang S-C. Topological quantum computation based on chiral  
527 Majorana fermions. *Proceedings of the National Academy of Sciences* 2018, **115**(43): 10938-  
528 10942.
- 529
- 530 9. Qi X-L, Hughes TL, Zhang S-C. Chiral topological superconductor from the quantum Hall state.  
531 *Physical Review B* 2010, **82**(18): 184516.
- 532
- 533 10. Huckestein B. Scaling theory of the integer quantum Hall effect. *Reviews of Modern Physics*  
534 1995, **67**(2): 357-396.
- 535
- 536 11. Sondhi SL, Girvin SM, Carini JP, Shahar D. Continuous quantum phase transitions. *Reviews of*  
537 *Modern Physics* 1997, **69**(1): 315-333.
- 538
- 539 12. Moreau N, Brun B, Somanchi S, Watanabe K, Taniguchi T, Stampfer C, *et al.* Upstream modes  
540 and antidots poison graphene quantum Hall effect. *Nature Communications* 2021, **12**(1): 4265.
- 541

- 542 13. Marguerite A, Birkbeck J, Aharon-Steinberg A, Halbertal D, Bagani K, Marcus I, *et al.* Imaging  
543 work and dissipation in the quantum Hall state in graphene. *Nature* 2019, **575**(7784): 628-  
544 633.
- 545
- 546 14. Maciejko J, Liu C, Oreg Y, Qi X-L, Wu C, Zhang S-C. Kondo Effect in the Helical Edge Liquid of  
547 the Quantum Spin Hall State. *Physical Review Letters* 2009, **102**(25): 256803.
- 548
- 549 15. Liu C, Culcer D, Wang Z, Edmonds MT, Fuhrer MS. Helical Edge Transport in Millimeter-Scale  
550 Thin Films of Na<sub>3</sub>Bi. *Nano Letters* 2020, **20**(9): 6306-6312.
- 551
- 552 16. Kane CL, Mele EJ. Quantum Spin Hall Effect in Graphene. *Physical Review Letters* 2005, **95**(22):  
553 226801.
- 554
- 555 17. Fu L, Kane CL, Mele EJ. Topological Insulators in Three Dimensions. *Physical Review Letters*  
556 2007, **98**(10): 106803.
- 557
- 558 18. Liu M, Wang W, Richardella AR, Kandala A, Li J, Yazdani A, *et al.* Large discrete jumps observed  
559 in the transition between Chern states in a ferromagnetic topological insulator. *Science*  
560 *Advances* 2016, **2**(7): e1600167.
- 561
- 562 19. Lee I, Kim CK, Lee J, Billinge SJL, Zhong R, Schneeloch JA, *et al.* Imaging Dirac-mass disorder  
563 from magnetic dopant atoms in the ferromagnetic topological insulator Cr<sub>x</sub>(Bi<sub>0.1</sub>Sb<sub>0.9</sub>)<sub>2</sub>-  
564 xTe<sub>3</sub>. *Proceedings of the National Academy of Sciences* 2015, **112**(5): 1316-1321.
- 565
- 566 20. Otrokov MM, Klimovskikh II, Bentmann H, Estyunin D, Zeugner A, Aliev ZS, *et al.* Prediction  
567 and observation of an antiferromagnetic topological insulator. *Nature* 2019, **576**(7787): 416-  
568 422.
- 569
- 570 21. Li J, Li Y, Du S, Wang Z, Gu B-L, Zhang S-C, *et al.* Intrinsic magnetic topological insulators in van  
571 der Waals layered MnBi<sub>2</sub>Te<sub>4</sub>-family materials. *Science Advances* 2019, **5**(6): eaaw5685.
- 572
- 573 22. Otrokov MM, Rusinov IP, Blanco-Rey M, Hoffmann M, Vyazovskaya AY, Ereemeev SV, *et al.*  
574 Unique Thickness-Dependent Properties of the van der Waals Interlayer Antiferromagnet  
575 MnBi<sub>2</sub>Te<sub>4</sub> Films. *Physical Review Letters* 2019, **122**(10): 107202.
- 576
- 577 23. Deng Y, Yu Y, Shi MZ, Guo Z, Xu Z, Wang J, *et al.* Quantum anomalous Hall effect in intrinsic  
578 magnetic topological insulator MnBi<sub>2</sub>Te<sub>4</sub>. *Science* 2020, **367**(6480): 895-900.
- 579
- 580 24. Bai Y, Li Y, Luan J, Liu R, Song W, Chen Y, *et al.* Quantized anomalous Hall resistivity achieved  
581 in molecular beam epitaxy-grown MnBi<sub>2</sub>Te<sub>4</sub> thin films. *arXiv preprint arXiv:220603773* 2022.
- 582
- 583 25. Garrity KF, Chowdhury S, Tavazza FM. Topological surface states of MnBi<sub>2</sub>Te<sub>4</sub> at finite  
584 temperatures and at domain walls. *Physical Review Materials* 2021, **5**(2): 024207.
- 585
- 586 26. Yuan Y, Wang X, Li H, Li J, Ji Y, Hao Z, *et al.* Electronic States and Magnetic Response of  
587 MnBi<sub>2</sub>Te<sub>4</sub> by Scanning Tunneling Microscopy and Spectroscopy. *Nano Letters* 2020, **20**(5):  
588 3271-3277.

589

590 27. Huang Z, Du M-H, Yan J, Wu W. Native defects in antiferromagnetic topological insulator  
591 MnBi<sub>2</sub>Te<sub>4</sub>. *Physical Review Materials* 2020, **4**(12): 121202.

592

593 28. Garnica M, Otrokov MM, Aguilar PC, Klimovskikh II, Estyunin D, Aliev ZS, *et al.* Native point  
594 defects and their implications for the Dirac point gap at MnBi<sub>2</sub>Te<sub>4</sub>(0001). *npj Quantum*  
595 *Materials* 2022, **7**(1): 7.

596

597 29. Liu M, Lei C, Kim H, Li Y, Frammolino L, Yan J, *et al.* Visualizing the interplay of Dirac mass gap  
598 and magnetism at nanoscale in intrinsic magnetic topological insulators. *Proceedings of the*  
599 *National Academy of Sciences* 2022, **119**(42): e2207681119.

600

601 30. Hor YS, Roushan P, Beidenkopf H, Seo J, Qu D, Checkelsky JG, *et al.* Development of  
602 ferromagnetism in the doped topological insulator Bi<sub>2</sub>-xMnxTe<sub>3</sub>. *Physical Review B* 2010,  
603 **81**(19): 195203.

604

605 31. Beidenkopf H, Roushan P, Seo J, Gorman L, Drozdov I, Hor YS, *et al.* Spatial fluctuations of  
606 helical Dirac fermions on the surface of topological insulators. *Nature Physics* 2011, **7**(12):  
607 939-943.

608

609 32. Trang CX, Li Q, Yin Y, Hwang J, Akhgar G, Di Bernardo I, *et al.* Crossover from 2D Ferromagnetic  
610 Insulator to Wide Band Gap Quantum Anomalous Hall Insulator in Ultrathin MnBi<sub>2</sub>Te<sub>4</sub>. *ACS*  
611 *Nano* 2021, **15**(8): 13444-13452.

612

613 33. Rienks EDL, Wimmer S, Sánchez-Barriga J, Caha O, Mandal PS, Růžička J, *et al.* Large magnetic  
614 gap at the Dirac point in Bi<sub>2</sub>Te<sub>3</sub>/MnBi<sub>2</sub>Te<sub>4</sub> heterostructures. *Nature* 2019, **576**(7787): 423-  
615 428.

616

617 34. Lüpke F, Pham AD, Zhao Y-F, Zhou L-J, Lu W, Briggs E, *et al.* Local manifestations of thickness-  
618 dependent topology and edge states in the topological magnet MnBi<sub>2</sub>Te<sub>4</sub>. *Physical Review B*  
619 2022, **105**(3): 035423.

620

621 35. Xu H-K, Gu M, Fei F, Gu Y-S, Liu D, Yu Q-Y, *et al.* Observation of Magnetism-Induced  
622 Topological Edge State in Antiferromagnetic Topological Insulator MnBi<sub>4</sub>Te<sub>7</sub>. *ACS Nano* 2022,  
623 **16**(6): 9810-9818.

624

625 36. Jia J, Marcellina E, Das A, Lodge MS, Wang B, Ho D-Q, *et al.* Tuning the many-body interactions  
626 in a helical Luttinger liquid. *Nature Communications* 2022, **13**(1): 6046.

627

628 37. Alpichshev Z, Analytis JG, Chu JH, Fisher IR, Chen YL, Shen ZX, *et al.* STM Imaging of Electronic  
629 Waves on the Surface of Bi<sub>2</sub>Te<sub>3</sub>: Topologically Protected Surface States and Hexagonal  
630 Warping Effects. *Physical Review Letters* 2010, **104**(1): 016401.

631

632 38. Collins JL, Tadich A, Wu W, Gomes LC, Rodrigues JNB, Liu C, *et al.* Electric-field-tuned  
633 topological phase transition in ultrathin Na<sub>3</sub>Bi. *Nature* 2018, **564**(7736): 390-394.

634

- 635 39. Padmanabhan H, Stoica VA, Kim PK, Poore M, Yang T, Shen X, *et al.* Large Exchange Coupling  
636 Between Localized Spins and Topological Bands in MnBi<sub>2</sub>Te<sub>4</sub>. *Advanced Materials* 2022,  
637 **34**(49): 2202841.  
638
- 639 40. Li B, Yan JQ, Pajerowski DM, Gordon E, Nedić AM, Sizyuk Y, *et al.* Competing Magnetic  
640 Interactions in the Antiferromagnetic Topological Insulator MnBi<sub>2</sub>Te<sub>4</sub>. *Physical Review Letters*  
641 2020, **124**(16): 167204.  
642
- 643 41. Sass PM, Kim J, Vanderbilt D, Yan J, Wu W. Robust A-Type Order and Spin-Flop Transition on  
644 the Surface of the Antiferromagnetic Topological Insulator MnBi<sub>2</sub>Te<sub>4</sub>. *Physical Review Letters*  
645 2020, **125**(3): 037201.  
646
- 647 42. Shikin A, Makarova T, Eryzhenkov A, Usachov DY, Estyunin D, Glazkova D, *et al.* Factors  
648 influencing the energy gap in topological states of antiferromagnetic MnBi<sub>2</sub>Te<sub>4</sub>. *arXiv preprint*  
649 *arXiv:220507501* 2022.  
650
- 651 43. Bac SK, Koller K, Lux F, Wang J, Riney L, Borisiak K, *et al.* Topological response of the  
652 anomalous Hall effect in MnBi<sub>2</sub>Te<sub>4</sub> due to magnetic canting. *npj Quantum Materials* 2022,  
653 **7**(1): 46.  
654
- 655 44. Yang S, Xu X, Zhu Y, Niu R, Xu C, Peng Y, *et al.* Odd-Even Layer-Number Effect and Layer-  
656 Dependent Magnetic Phase Diagrams in MnBi<sub>2</sub>Te<sub>4</sub>. *Physical Review X* 2021, **11**(1): 011003.  
657
- 658 45. He K, Xue Q-K. The Road to High-Temperature Quantum Anomalous Hall Effect in Magnetic  
659 Topological Insulators. *SPIN* 2019, **09**: 1940016.  
660
- 661 46. Fu H, Liu C-X, Yan B. Exchange bias and quantum anomalous Hall effect in the MnBi<sub>2</sub>Te<sub>4</sub>/CrI<sub>3</sub>  
662 heterostructure. *Science Advances* 2020, **6**(10): eaaz0948.  
663
- 664 47. Otrokov MM, Menshchikova TV, Vergniory MG, Rusinov IP, Yu Vyazovskaya A, Koroteev YM,  
665 *et al.* Highly-ordered wide bandgap materials for quantized anomalous Hall and  
666 magnetoelectric effects. *2D Materials* 2017, **4**(2): 025082.  
667
- 668 48. Li Q, Trang CX, Wu W, Hwang J, Cortie D, Medhekar N, *et al.* Large Magnetic Gap in a Designer  
669 Ferromagnet–Topological Insulator–Ferromagnet Heterostructure. *Advanced Materials* 2022,  
670 **34**(21): 2107520.  
671
- 672 49. Bhattacharyya S, Akhgar G, Gebert M, Karel J, Edmonds MT, Fuhrer MS. Recent Progress in  
673 Proximity Coupling of Magnetism to Topological Insulators. *Advanced Materials* 2021, **33**(33):  
674 2007795.  
675
- 676 50. Zhu T, Bishop AJ, Zhou T, Zhu M, O’Hara DJ, Baker AA, *et al.* Synthesis, Magnetic Properties,  
677 and Electronic Structure of Magnetic Topological Insulator MnBi<sub>2</sub>Se<sub>4</sub>. *Nano Letters* 2021,  
678 **21**(12): 5083-5090.  
679  
680  
681

682

## Supporting Information

# 683 Imaging the breakdown and restoration of topological protection in 684 magnetic topological insulator $\text{MnBi}_2\text{Te}_4$

685

686 Qile Li<sup>1,2\*</sup>, Iolanda Di Bernardo<sup>1,2</sup>, Johnathon Maniatis<sup>1</sup>, Daniel McEwen<sup>1,2</sup>, Amelia D. Celorrio<sup>1,2</sup>,  
687 Mohammad T. H. Bhuiyan<sup>1</sup>, Mengting Zhao<sup>1,2,3</sup>, Anton Tadich<sup>3</sup>, Liam Watson<sup>1,2</sup>, Benjamin Lowe<sup>1,2</sup>,  
688 Thi-Hai-Yen Vu<sup>1</sup>, Chi Xuan Trang<sup>1,2</sup>, Jinwoong Hwang<sup>4,5</sup>, Sung-Kwan Mo<sup>4</sup>, Michael S. Fuhrer<sup>1,2</sup>,  
689 Mark T. Edmonds<sup>1,2,6\*</sup>

690

691 <sup>1</sup>School of Physics and Astronomy, Monash University, Clayton, VIC, Australia

692 <sup>2</sup>ARC Centre for Future Low Energy Electronics Technologies, Monash University, Clayton, VIC,  
693 Australia

694 <sup>3</sup>Australian Synchrotron

695 <sup>4</sup>Advanced Light Source, Lawrence Berkeley National Laboratory, Berkeley, CA, 94720 USA

696 <sup>5</sup>Department of Physics and Institute of Quantum Convergence Technology, Kangwon National  
697 University, Chuncheon, 24341, Republic of Korea

698 <sup>6</sup>ANFF-VIC Technology Fellow, Melbourne Centre for Nanofabrication, Victorian Node of  
699 the Australian National Fabrication Facility, Clayton, VIC 3168, Australia

700

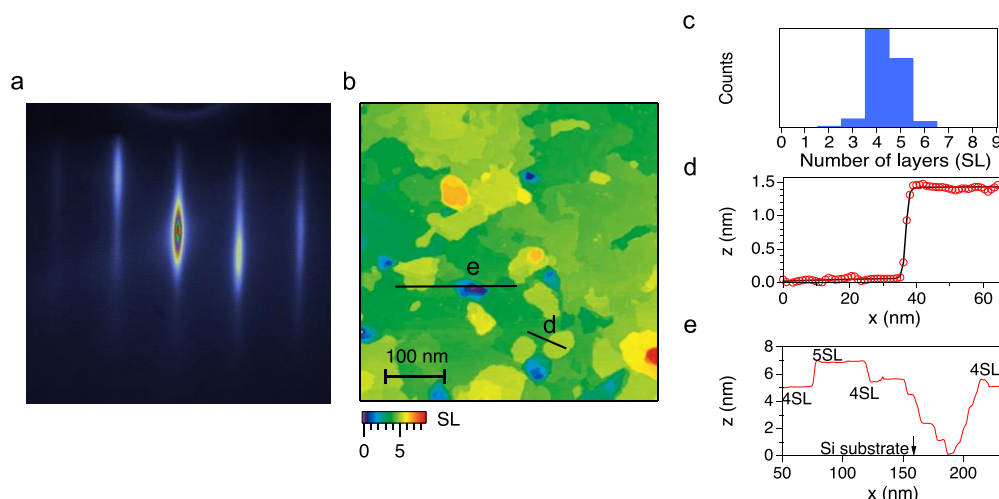
701 \*Corresponding Author [mark.edmonds@monash.edu](mailto:mark.edmonds@monash.edu) and [qile.li@monash.edu](mailto:qile.li@monash.edu)

702

### 703 Table of Contents

- 704 1. Structure and surface characterization of 5 SL  $\text{MnBi}_2\text{Te}_4$  epitaxial film
- 705 2. Doping shift due to different Si (111) substrates.
- 706 3. Schematics and determination of  $\text{Bi}_{\text{Mn}}$  defects
- 707 4. Determination of Dirac band gap and gap center from  $dI/dV$  spectrum
- 708 5. Bias dependent and set point current dependent STS measurements
- 709 6. Topography image and  $dI/dV$  map of the 5SL to 4SL edge in Figure 2 at other bias value.
- 710 7. Topography image and  $dI/dV$  map of a 4SL to 3SL edge.
- 711 8. Visualizing the gapless edge state and its coupling to bulk metallic states
- 712 9. Representative  $dI/dV$  spectra from STS map around  $\text{Mn}_{\text{Bi}}$  defects
- 713 10. Topography scan of the area in Figure 4 to show the alignment of the scan region
- 714 11. Figure 4 statistical analysis of regions with unsuppressed CB at both 0T and 1T
- 715 12. Magnetic field dependent Dirac gap map
- 716 13. Dirac band gap maps from region with large number of  $\text{Bi}_{\text{Mn}}$  defects.



1. Structure and surface characterization of 5 SL  $\text{MnBi}_2\text{Te}_4$  epitaxial film

718

719

**Figure S1 | Structure and surface characterization of ultra-thin  $\text{MnBi}_2\text{Te}_4$  epitaxial film.**

720

(a) Reflection high energy electron diffraction of the thin film showing strong sharp streaks which

721

indicates high crystallinity. (b) STM topography scan on a  $500 \times 500$  nm area (-2 V, 20 pA). (c)

722

Histogram of number of SLs from (b) which shows majority of 4 SL terrace (green) with regions of 5

723

SL terrace (yellow). The thickness is determined from the depth of pinholes (dark blue and purple

724

regions) which represent the Si substrate. (d) A line profile extracted from one of the 4 SL-5 SL step

725

edges as marked by the black line in (b) and fitting to an edge function, which yields a step edge of

726

1.39 nm. (e) A line profile extracted across a pin hole to show the thickness of terraces as marked by

727

the black line in (b).

728

729

730

731

732

733

734

735

736

737

738

739

740

741

742

743

744

745

746

747

748

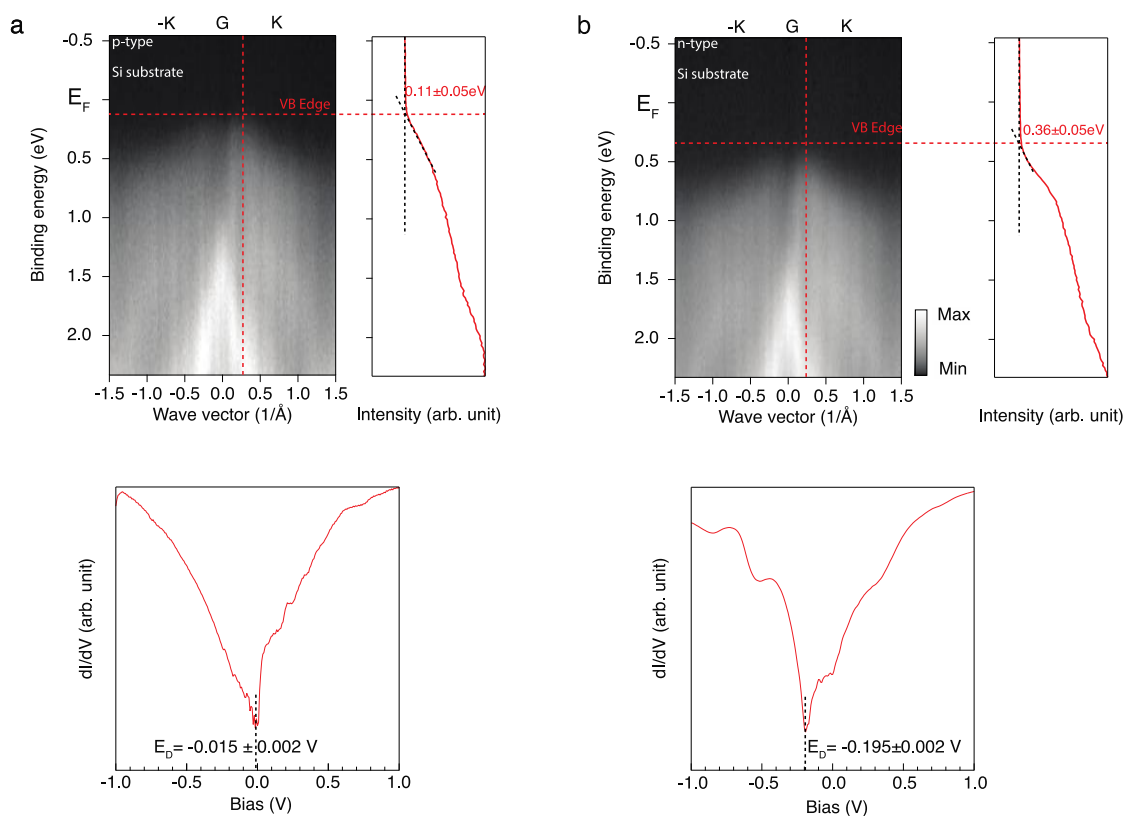
749

750

751

752

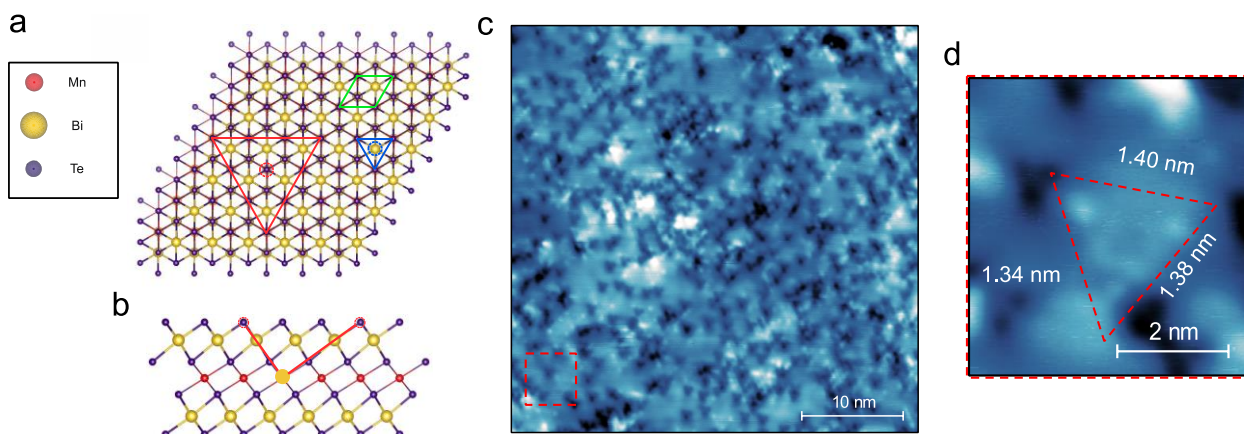
753 2. Doping shift due to different Si(111) substrates.



754  
 755 **Figure S2 | ARPES spectra and representative scanning tunnelling spectroscopy (STS) spectra**  
 756 **of 5SL MnBi<sub>2</sub>Te<sub>4</sub> grown on (a) p-type and (b) n-type silicon substrates respectively using He-II**  
 757 **light source ( $h\nu = 21.2\text{eV}$ ).** The Dirac cone is not visible in the ARPES spectra because of the low  
 758 photon flux of the helium lamp. The energy distribution curve is taken at the wave vector marked by  
 759 the red dashed lines and are plotted on the right of each spectrum. The edge of valence bands is  
 760 determined from ARPES and the Dirac point energy is determined from the minima in the STS spectra,  
 761 which are used for estimating the doping level of the samples. A doping level difference between the  
 762 two types of Si (111) substrates is  $\sim 180\text{ meV}$ .

763  
 764  
 765  
 766  
 767  
 768  
 769  
 770  
 771  
 772  
 773  
 774  
 775  
 776  
 777  
 778  
 779  
 780

781 3. Schematics and determination of  $\text{Bi}_{\text{Mn}}$  defects

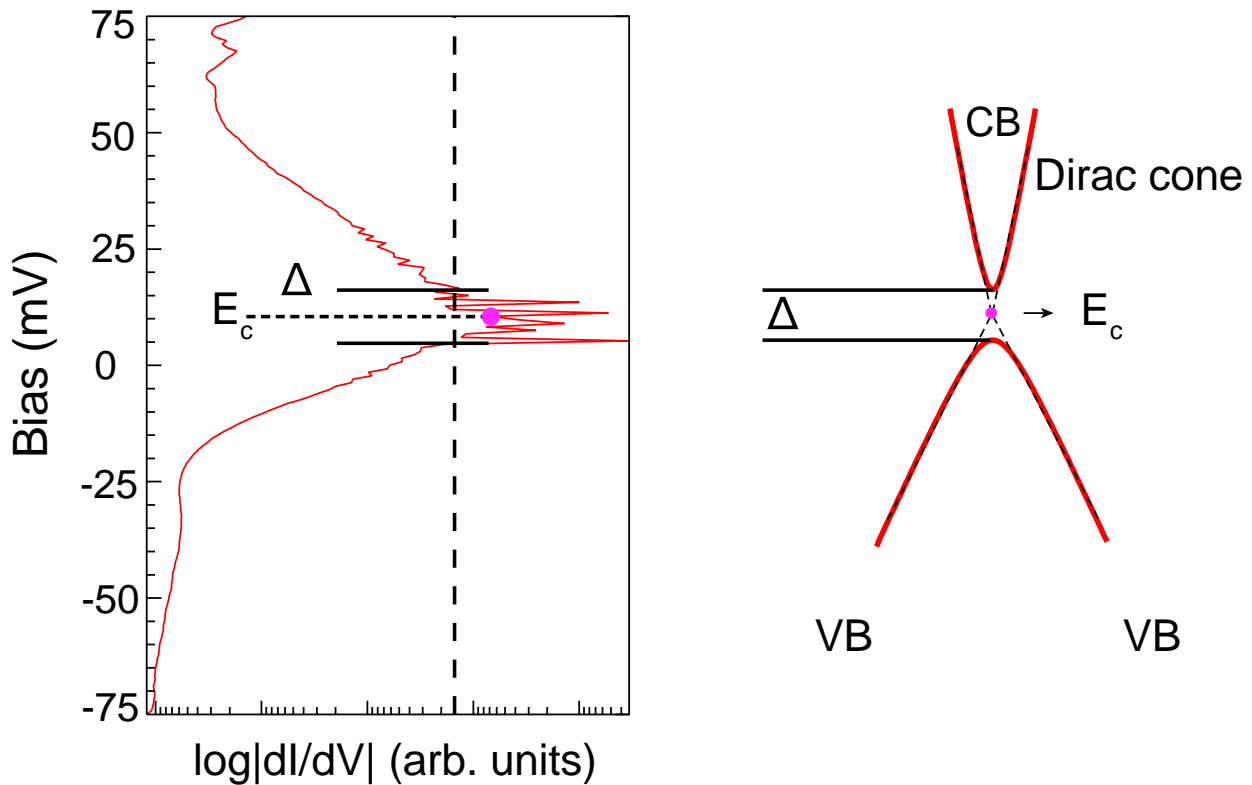


782  
 783 **Figure S3 | Schematics and determination of  $\text{Bi}_{\text{Mn}}$  defects.** (a) Top view of the crystal structure with  
 784 primitive cell (green),  $\text{Mn}_{\text{Bi}}$  defect (blue) and  $\text{Bi}_{\text{Mn}}$  defect (red) marked. (b) Side view of the  $\text{Bi}_{\text{Mn}}$   
 785 defect in a SL. The Te atoms on the very top appear as bright triangles at positive bias because of DOS  
 786 propagated along Te  $p_z$  orbitals centered around  $\text{Bi}_{\text{Mn}}$  defect. The three Te atoms appear to be more  
 787 positively charged due to the extra charge from a  $\text{Bi}^{3+}$  ion replacing  $\text{Mn}^{2+}$  ion. (c) Topography scan on  
 788 a  $40 \times 40$  nm area (+1.7 V, 80 pA) showing  $\text{Bi}_{\text{Mn}}$  defects on an atomically flat terrace. (d) A zoom-in  
 789 image of the selected region marked by red box in (c) for extracting dimensions of defects. The length  
 790 of the triangle's edge is around 1.35 nm which is close to the theoretical value of 1.31 nm. The same  
 791 orientation of  $\text{Mn}_{\text{Bi}}$  dark triangles and  $\text{Bi}_{\text{Mn}}$  bright triangles also matches the schematics (a).

792  
 793  
 794  
 795  
 796  
 797  
 798  
 799  
 800  
 801  
 802  
 803  
 804  
 805  
 806  
 807  
 808  
 809  
 810  
 811  
 812  
 813  
 814  
 815

816  
817

#### 4. Determination of Dirac band gap and gap center from $dI/dV$ spectrum



818  
819  
820  
821  
822  
823  
824  
825  
826

**Figure S4| Determination of Dirac band gap and gap center from  $dI/dV$  spectrum.** **Left**, a  $dI/dV$  spectrum taken on a 5 SL  $\text{MnBi}_2\text{Te}_4$  terrace showing a gap in the Dirac states. **Right**, a schematic of the Dirac cone corresponding to the  $dI/dV$  spectrum on the left. The Dirac cone in 5 SL  $\text{MnBi}_2\text{Te}_4$  is lifted out of VB and resides between bulk conduction band (CB) and bulk valence band (VB). The Dirac gap is extracted based on the noise floor of the  $dI/dV$  spectrum (black dashed line). The width of the region between valence and conduction band edges corresponds to the size of Dirac gap  $\Delta$  as illustrated on the right figure.

827  
828  
829  
830  
831

To extract the Dirac gap from STS spectra, the edges of valence band and conduction band are determined from the spectrum as the onset of  $dI/dV$  intensity above the noise floor (black dashed line in **Figure S4** left). A logarithmic scale is chosen for  $dI/dV$  intensity axis to better account for the sudden change of intensity near the band edge. The local doping level can be estimated from the center of Dirac gap which can be calculated using

832

$$E_c = \frac{\int f(\mathbf{r}, E) E dE}{\int f(\mathbf{r}, E) dE}$$

833  
834  
835  
836  
837  
838  
839

where  $f(\mathbf{r}, E)=1$  if STS curve  $g(\mathbf{r}, E) < \text{noise floor}$  and  $f(\mathbf{r}, E)=0$  otherwise<sup>19</sup>. This is essentially averaging the position of center of gap and is equivalent to extrapolating the gapped Dirac bands as shown in **Figure S4** right. Since the Dirac cone is now gapped by magnetic order and Dirac point no longer exists, the gap center (purple dot) is a good measure of the local doping shift by defects.

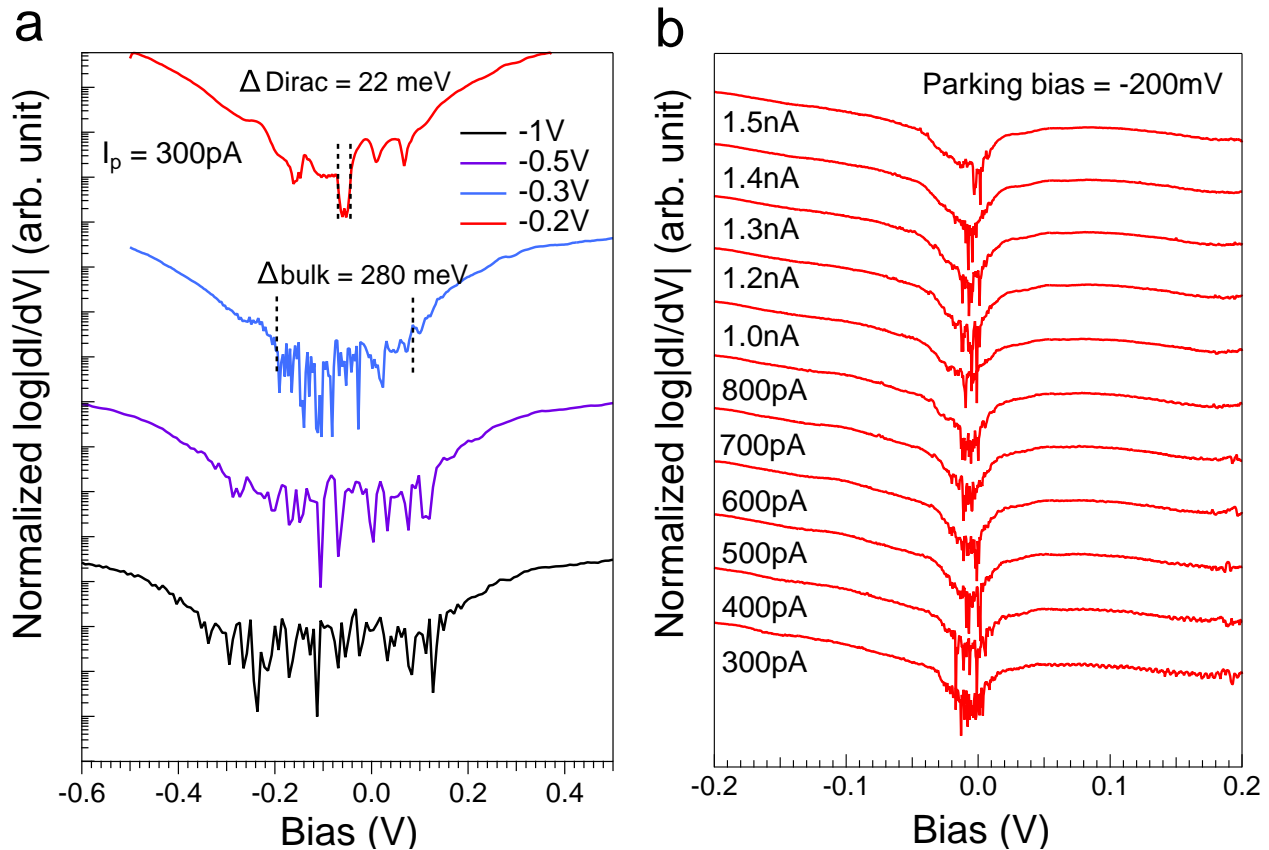
840

841

## 5. Bias dependent and set point current dependent STS measurements

842

843



844

845

846

847

848

849

850

851

852

853

854

855

856

857

858

859

860

861

862

863

864

865

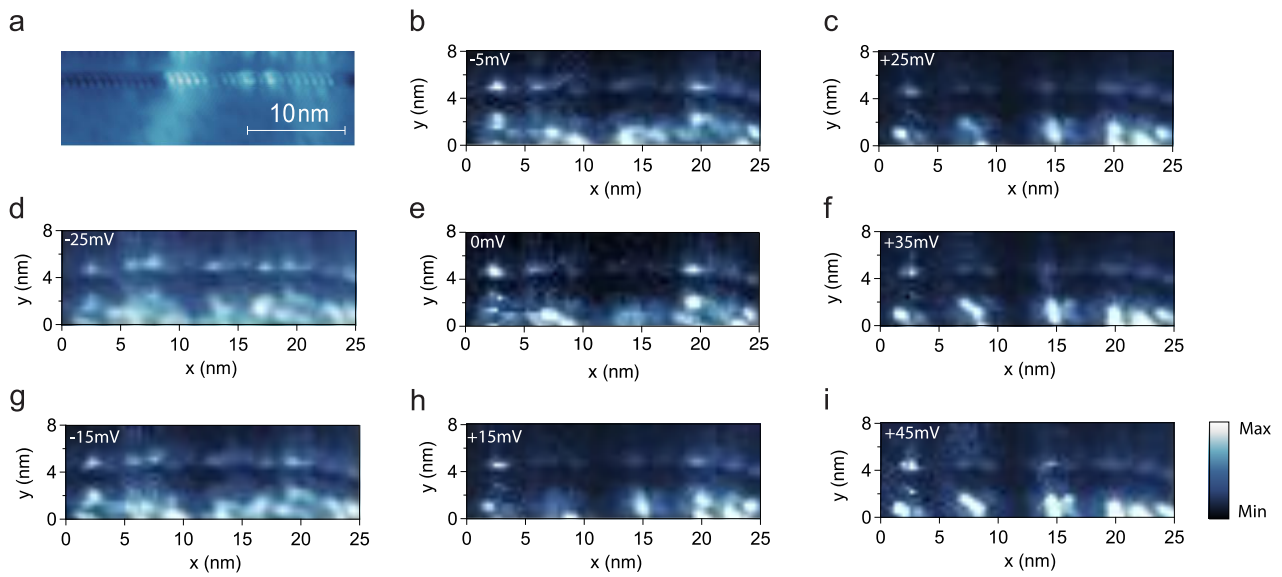
866

**Figure S5 | Bias dependent and set point current dependent STS measurements.** (a) STS spectra taken at different bias, the tip-sample tunneling junction decreases as the bias voltage decreases bias, resulting in a stronger signal which is necessary to observe the Dirac bands in  $dI/dV$ . (b) STS spectra taken at various set point current and fixed parking bias of -200 mV showing a Dirac gap. The band edge position shows minimal shift at different set point current and bias, indicating minimal tip induced band bending.

As shown in **Figure S5(a)**, the STS spectrum on the terrace only shows a large bulk gap at parking bias of -1 V. As the tip is parked closer to the surface by decreasing bias, more features in the spectrum, including surface states and Dirac band gap, can be resolved within the bulk gap. Therefore, we choose parking bias of typical value -0.2 V and 300 pA for our STS maps. In **Figure S5(b)**, STS spectra taken on the same location and fixed bias but with varying set point current are plotted and offset manually. From set point current of 300 pA to 1.5 nA, there is no significant shift of band edges or increase of band gap. In the case of tip induced band bending, increasing the set point current will increase the band bending and lead to increase of band gap. Apparently, the most noticeable change in the **Figure S5(b)** is reduced noise in the spectra while the overall shape and position of the band edge stay the unchanged. Therefore, we can rule out contribution from tip induced band bending to the band gap.

867  
868  
869  
870

6. Topography image and  $dI/dV$  map of the 5SL to 4SL edge in Figure 2 at other bias values.

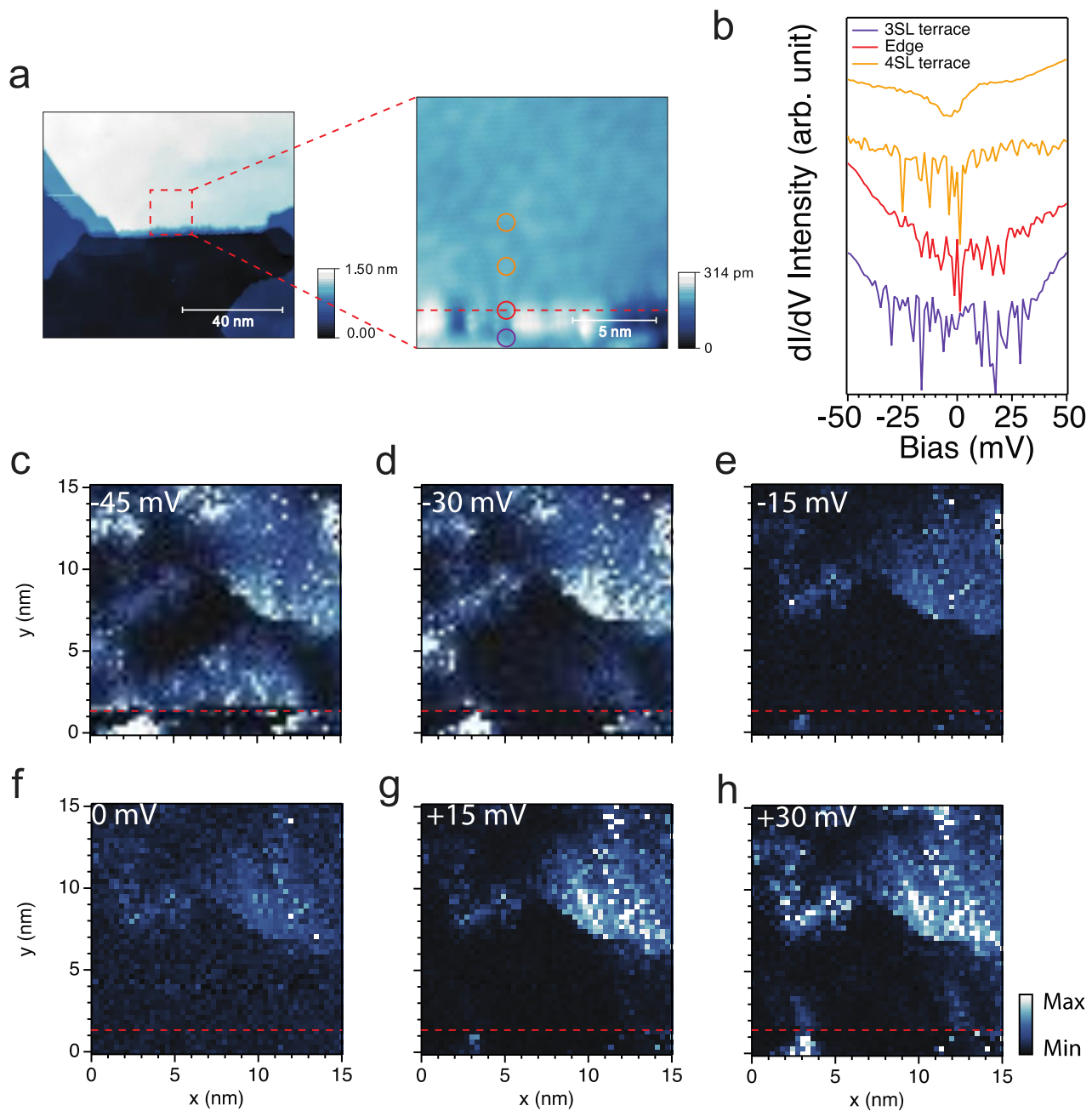


871  
872  
873  
874  
875  
876  
877  
878  
879  
880  
881  
882  
883  
884  
885  
886  
887  
888  
889  
890  
891  
892  
893  
894  
895  
896  
897  
898  
899  
900  
901

**Figure S6| (a) Topography image (-1 V, 30 pA) and (b)-(i)  $dI/dV$  maps (-0.15 V, 400 pA) of the edge in Figure 2 at other bias values.**

902  
903

### 7. Topography image and $dI/dV$ map of a 4SL to 3SL edge.

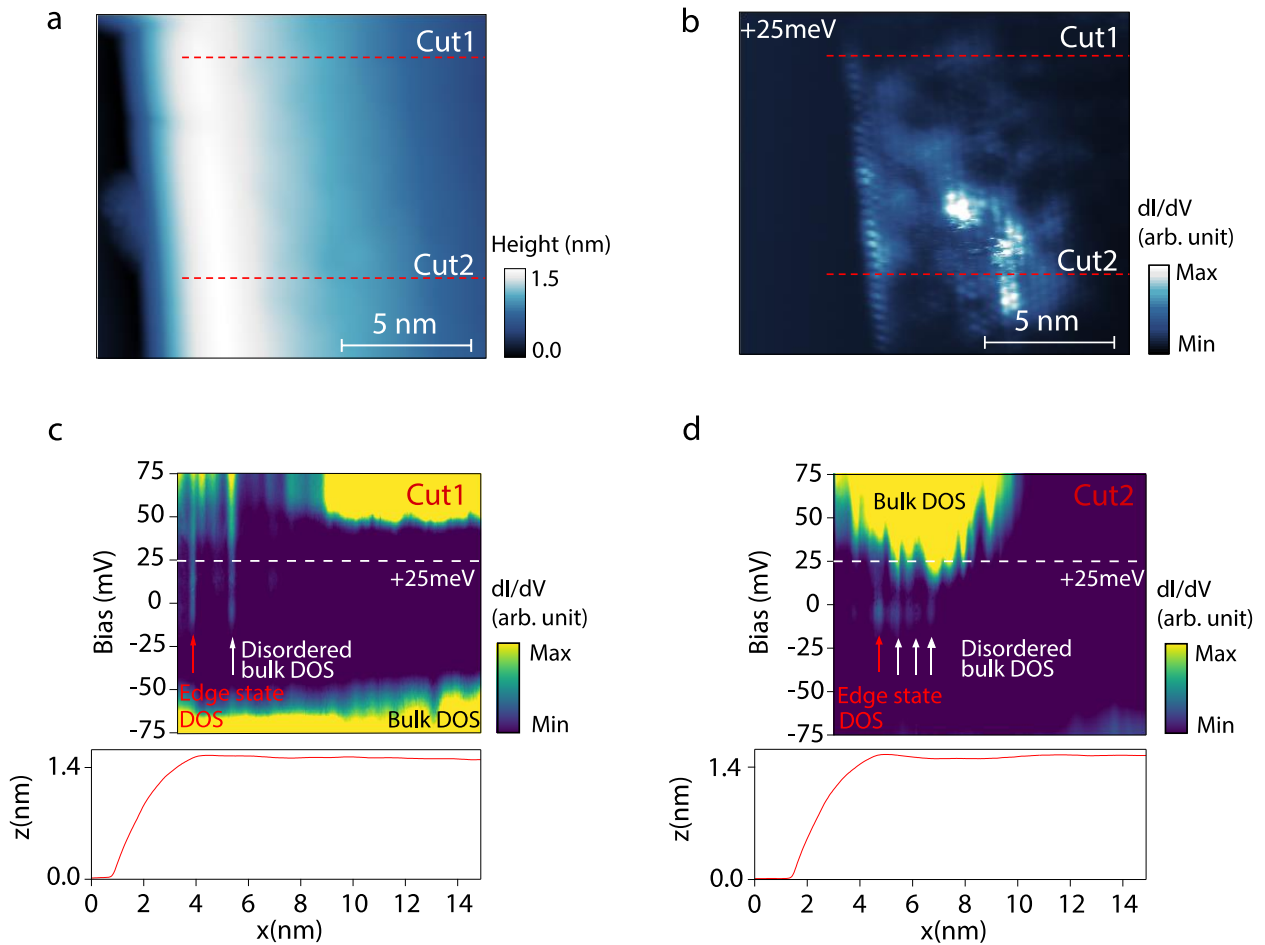


904  
905  
906  
907  
908  
909  
910  
911  
912  
913  
914  
915

**Figure S7 |  $dI/dV$  maps on an even-to-odd edge at several bias across the band gap. (a) topography scans (-2.5 V, 20 pA) of the edge, atomic-resolution scan (-2.5V, 20 pA) where maps are taken and (b) STS spectra (-0.15V, 400 pA) at locations marked. The terrace edge is marked by the red dash line. (c) to (h)  $dI/dV$  maps (-0.15V, 400 pA) at various bias with location of edge marked.**

916  
917

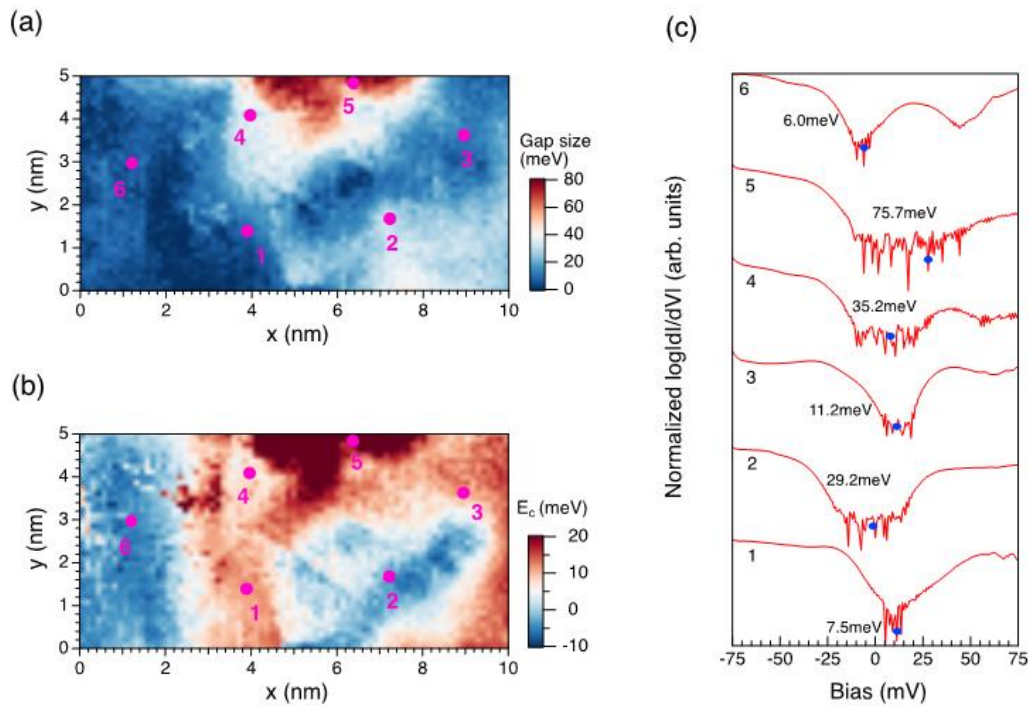
## 8. Visualizing the gapless edge state and its coupling to bulk metallic states.



918  
919  
920  
921  
922  
923  
924  
925  
926  
927  
928  
929  
930  
931  
932  
933  
934  
935  
936  
937  
938

**Figure S8 | Visualizing the gapless edge state and its coupling to bulk metallic states.** (a) Topography image (-1 V, 50 pA) taken across a step edge from 4 SL to 5 SL  $\text{MnBi}_2\text{Te}_4$ . (b)  $dI/dV$  map at +25 mV bias (40 pA) in the same region as (a) to show the spatial distribution of the edge state. (c),(d)  $dI/dV$  spectra (-0.15V, 350pA) and height profile taken across the edge from top of the area and bottom of the area respectively marked by red dashed lines. The horizontal axis of the spectra is aligned with the height profile. The edge state is marked by red arrow and other peaks are attributed to disordered bulk states which is marked by white arrows. The white horizontal dashed line shows the bias at which (b) is taken.



9. Representative  $dI/dV$  spectra from STS map around  $Mn_{Bi}$  defects

940

941

942 **Figure S9 | Representative  $dI/dV$  spectra from STS map around  $Mn_{Bi}$  defects.** (a) Band gap map943 extracted from  $dI/dV$  spectra (-0.1 V, 800 pA) with some locations where STS shown marked in green.944 (b) Gap center map extracted from  $dI/dV$  spectra. (c) Stack plot of  $dI/dV$  spectra taken from locations945 in (a)-(b), where band gap values are marked on each  $dI/dV$  spectrum, and gap center positions946 calculated using method discussed in **Figure S4** are marked by blue points.

947

948

949

950

951

952

953

954

955

956

957

958

959

960

961

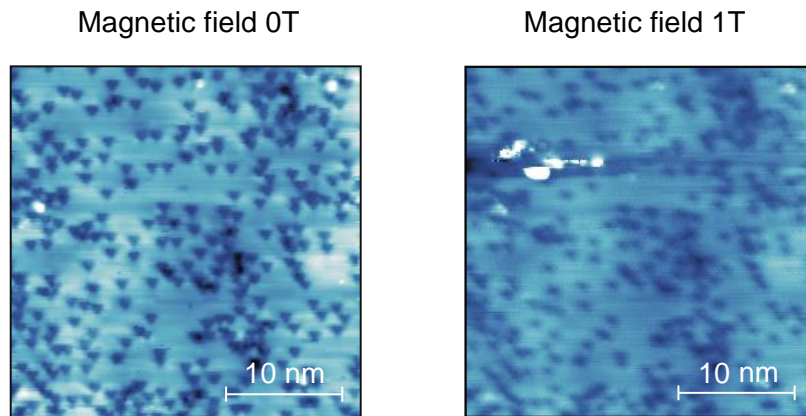
962

963

964

965  
966

10. Topography scan of the area in Figure 4 to show the alignment of the scan region.



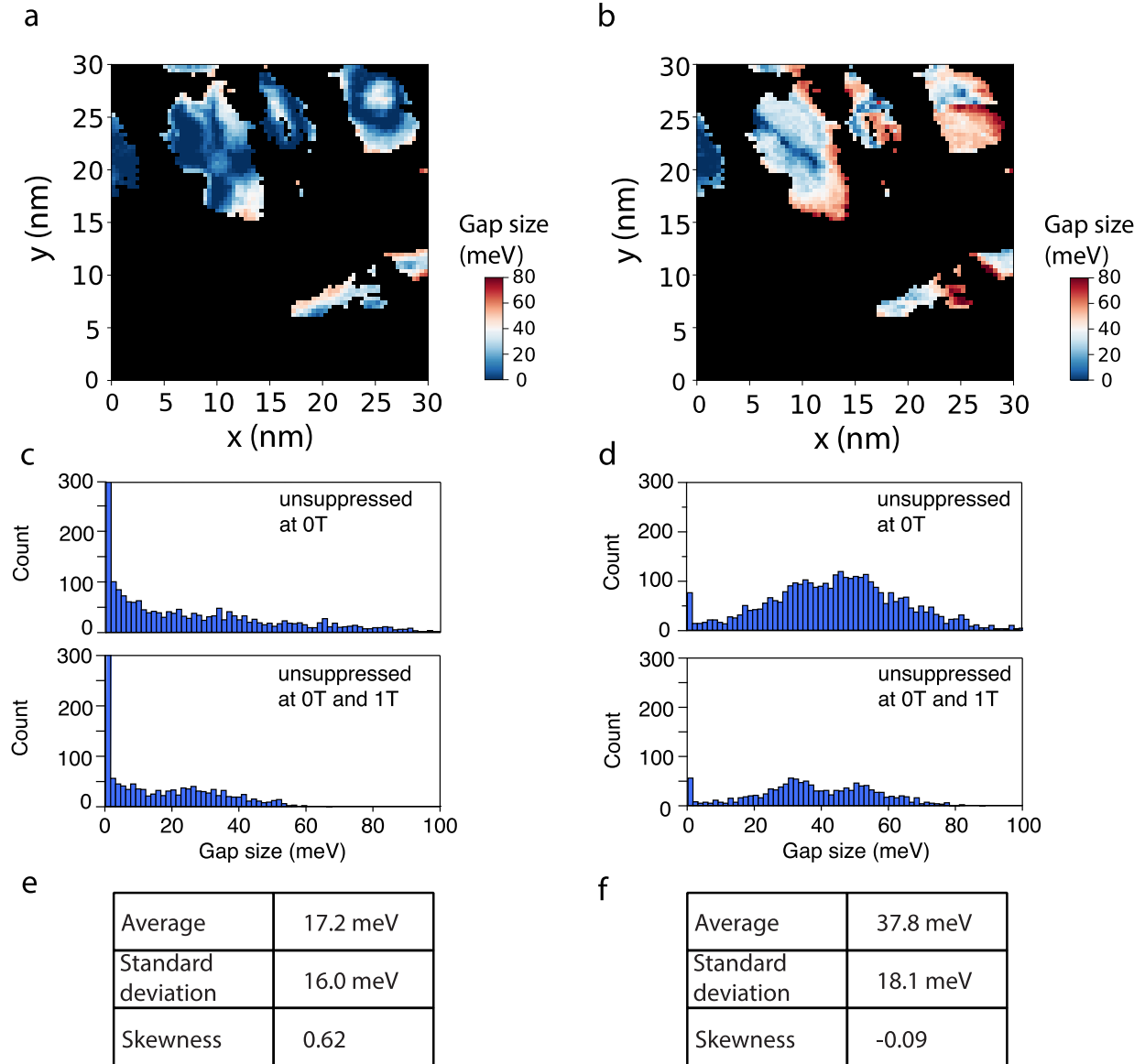
967  
968

**Figure S10 | Topography scans (both taken at -0.5 V, 100 pA) of the region for band gap mapping in Figure 4 at 0T and 1T.**

971  
972  
973  
974  
975  
976  
977  
978  
979  
980  
981  
982  
983  
984  
985  
986  
987  
988  
989  
990  
991  
992  
993  
994  
995  
996  
997  
998  
999  
1000

1001  
1002

11. Figure 4 statistical analysis of regions with unsuppressed CB at both 0T and 1T



1003  
1004  
1005  
1006  
1007  
1008  
1009  
1010  
1011  
1012  
1013  
1014  
1015  
1016  
1017  
1018

**Figure S11 | Statistical analysis of regions with unsuppressed CB at both 0T and 1T.** (a)-(b),  $E_{g,ex}$  map. (c)-(d), their corresponding histogram, and (e)-(f), statistical information extracted from the histograms.

In **Figure S11**, the histograms are taken from regions where the conduction band intensity is not suppressed at 0T or 1T. The analysis shows similar results as in **Figure 4**, with an increase in the average band gap size of 20.6meV. Interestingly the histogram in **Fig. S11(d)** appears to be more bimodal where the lower gap size mode corresponds to the weight shift from gapless to medium size gap and upper mode corresponds to shift from regions with medium size gap to fully gapped ones in a 1T magnetic field. Overall, regardless of the analysis method, this region shows significant increase of Dirac gap and reduction of skewness relative to a normal distribution in a 1T magnetic field.

## 12. Magnetic field dependent Dirac gap map

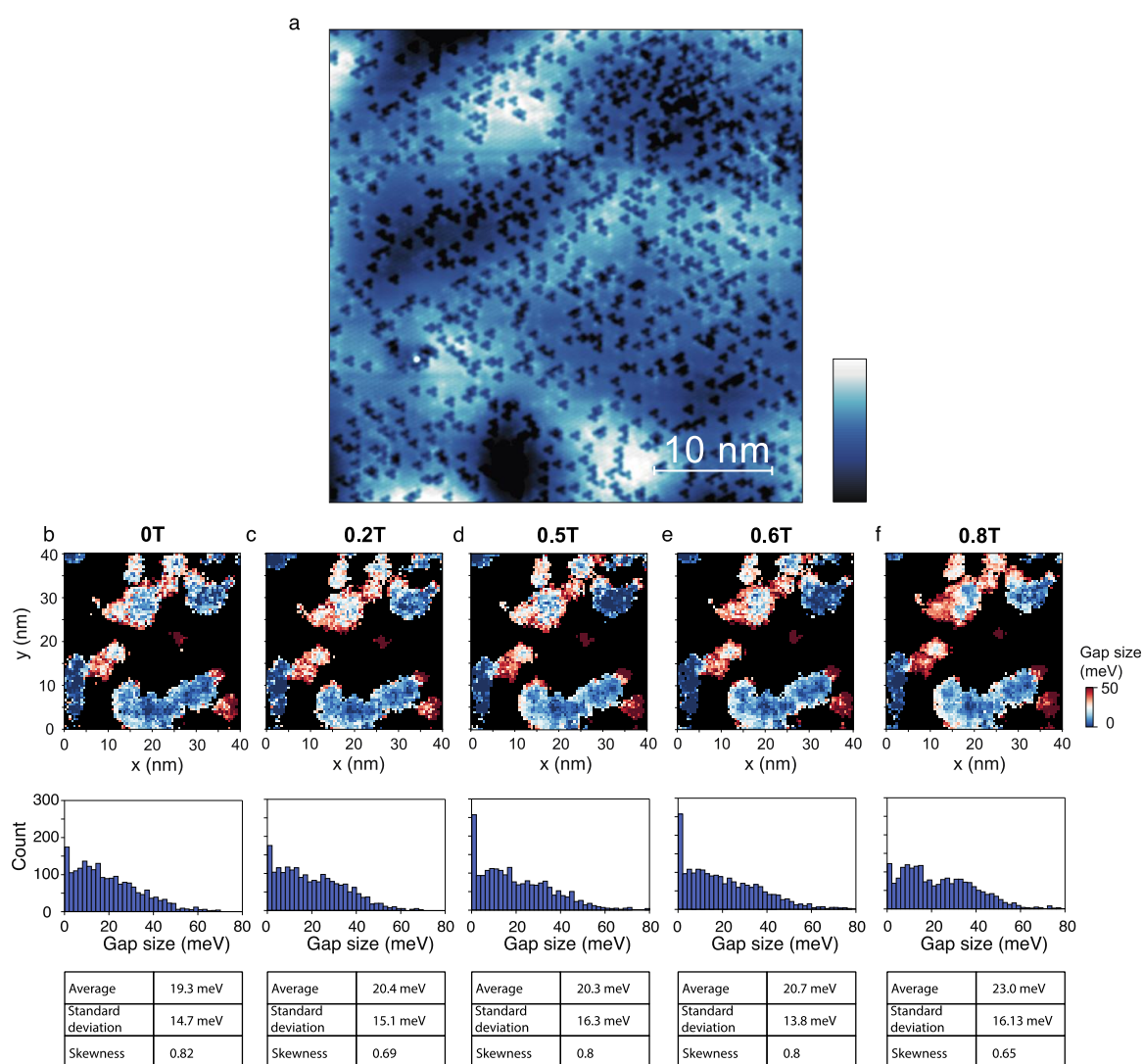


**Figure S12 | Magnetic field dependent Dirac gap map and their corresponding histogram and statistical information. (a) Topography scan of the map area ( $40 \times 40$  nm,  $-1$  V,  $100$  pA). (b) – (f) Magnetic field dependent band gap maps ( $-0.15$  V,  $400$  pA,  $75 \times 75$  pixels), their histograms and statistic information.**

The evolution of the histogram is very small below  $0.6$ T and there is a sudden increase of count of gapless state. We assign this anomaly to the realigning process of  $\text{Mn}^{2+}$  moments that are initially oriented opposite to magnetic field due to magnetic disorder. The reduction of the effective out-of-plane magnetization in some regions results in the temporary increase of gapless state. At  $0.8$ T, the count of gapless states is greatly reduced, and the bimodal feature emerges in the histogram, which is similar to the bimodal behavior in **Fig.S11(d)**.

1020

1021

1022

1023

1024

1025

1026

1027

1028

1029

1030

1031

1032

1033

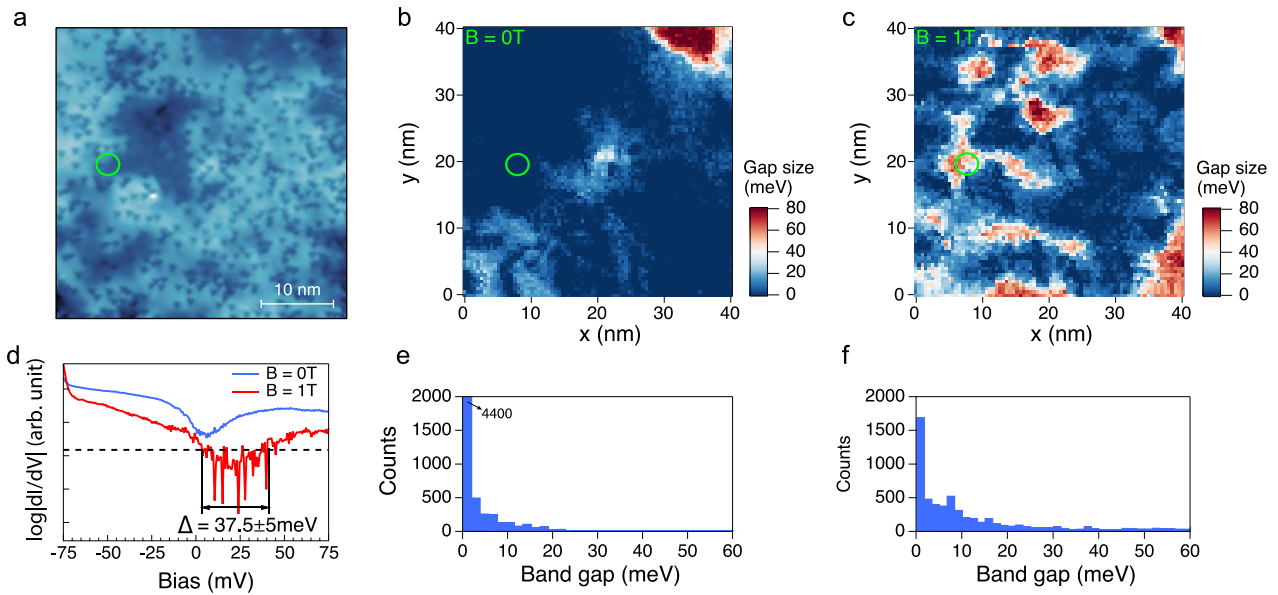
1034

1035

1036

1037

1038

13. Dirac band gap maps from region with large number of  $\text{Bi}_{\text{Mn}}$  defects

1040

1041

**Figure S13 | Dirac band gap maps with/without magnetic field showing band gap fluctuation from region with  $\text{Bi}_{\text{Mn}}$  defects.** (a) Topography scan of the same area as in Figure S3 (80 pA, -1 V). (b) Spatial dependent of Dirac band gap modulation at B=0 T (-0.17V, 400 pA). (c) Dirac band gap map taken at 1 T field (-0.17 V, 400 pA) where gapped regions now form pattern (blue). (d)  $dI/dV$  spectra taken from the green circle in (a) at B=0 T (blue) and 1T (red). An exchange gap is opened in 1 T field where exchange coupling is enhanced by the external field. (e) Band gap histogram extracted from (b) which shows significant counts from gapless regions (dark red in b). (f) Histogram extracted from (c) which shows that Dirac band gaps are increased with a drastic decrease of gapless regions.

1049

**Figure S13** shows magnetic field dependent Dirac band gap maps from a region with a large concentration of  $\text{Bi}_{\text{Mn}}$  defects. Clearly, upon applying a perpendicular magnetic field of 1 T, the band gap map shows up more regions with small band gap around 10 meV. In some regions the band gap has increased from gapless to moderate value of 40 meV. As shown in (f), there is now visible counts from regions with gap larger than 30 meV. Statistical analysis on the maps in (b) and (c) shows an increase of average band gap value from 4.6 meV to 14.8 meV. The emerging counts from moderate band gap region results in an increase of standard deviation from 12.5 meV to 18.3 meV and similar to the results in **Figure 4**, the restoration of Dirac band gap is accompanied by decreasing skewness from 4.5 to 1.5. The results in **Figure S13** indicates that regions with large numbers of  $\text{Bi}_{\text{Mn}}$  defects are typically much more gapless and the exchange gap can be restored partially with a perpendicular magnetic field of 1 T. Because  $\text{Bi}_{\text{Mn}}$  defects are non-magnetic, the pattern emerged in **Figure S13c** reflects the change of magnetic disorder in the center  $\text{Mn}^{2+}$  layer. The amount of  $\text{Bi}_{\text{Mn}}$  defects (see **Figure S3c**) could be responsible for the magnetic disorder.

1063

1064

1065

1066